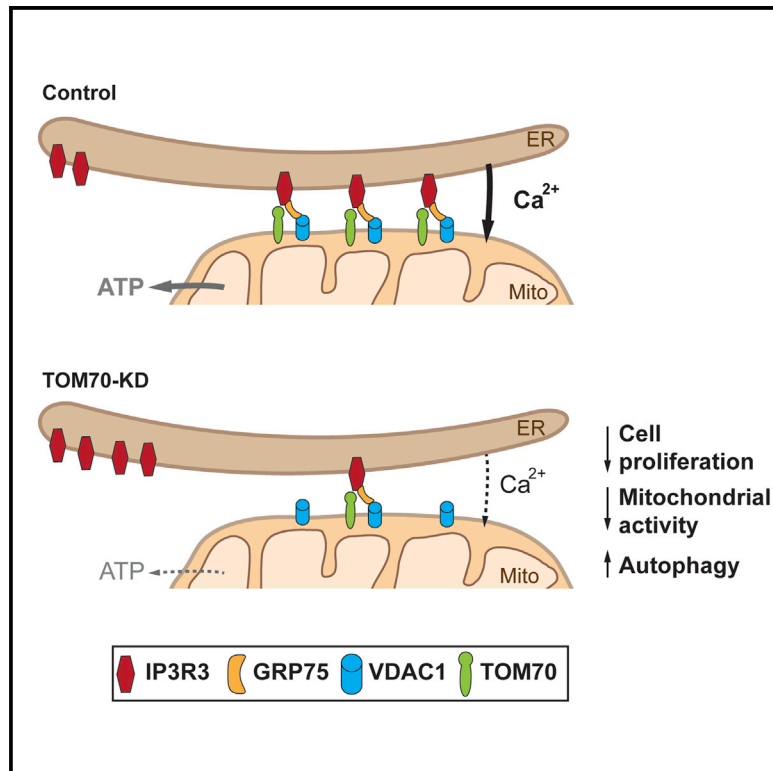# TOM70 Sustains Cell Bioenergetics by Promoting IP3R3-Mediated ER to Mitochondria Ca^{2+} Transfer

Graphical Abstract

Authors

Riccardo Filadi, Nuno Santos Leal,
Bernadette Schreiner, ..., Tito Calì,
Paola Pizzo, Maria Ankarcrona

Correspondence

paola.pizzo@unipd.it (P.P.),
maria.ankarcrona@ki.se (M.A.)

In Brief

Filadi et al. show that TOM70, a component of the mitochondrial translocase of the outer membrane, has an IP3R3-dependent but translocase-independent function that sustains cell bioenergetics. TOM70 clusters at ER-mitochondria contacts, recruits IP3R3, and promotes inter-organelle Ca^{2+} transfer, bioenergetics, and cell proliferation.

Highlights

- TOM70 clusters at ER-mitochondria contact sites

- TOM70 interacts with IP3R3 and recruits it close to mitochondria

- TOM70 promotes IP3-dependent ER to mitochondria Ca^{2+} transfer

- Mitochondrial Ca^{2+} signal promoted by TOM70 sustains cell bioenergetics

CellPress

CellPress

TOM70 Sustains Cell Bioenergetics by Promoting IP3R3-Mediated ER to Mitochondria Ca^{2+} Transfer

Riccardo Filadi,[1,4] Nuno Santos Leal,[2,4] Bernadette Schreiner,[2,4] Alice Rossi,[1] Giacomo Dentoni,[2]
Catarina Moreira Pinho,[2] Birgitta Wiehager,[2] Domenico Cieri,[1] Tito Calì,[1] Paola Pizzo,[1,3,5,*] and Maria Ankarcrona[2,*]
[1]Department of Biomedical Sciences, University of Padua, Via U. Bassi 58/B, 35121 Padua, Italy
[2]Center for Alzheimer Research, Division of Neurogeriatrics, Department of Neurobiology, Care Sciences and Society, Novum 5th Floor,
Karolinska Institutet, 141 57 Huddinge, Sweden
[3]Neuroscience Institute - Italian National Research Council (CNR), 35121 Padua, Italy
[4]These authors contributed equally
[5]Lead Contact
*Correspondence: paola.pizzo@unipd.it (P.P.), maria.ankarcrona@ki.se (M.A.)
https://doi.org/10.1016/j.cub.2017.12.047

SUMMARY

The mitochondrial translocase of the outer membrane (TOM) is a protein complex that is essential for the post-translational import of nuclear-encoded mitochondrial proteins. Among its subunits, TOM70 and TOM20 are only transiently associated with the core complex, suggesting their possible additional roles within the outer mitochondrial membrane (OMM). Here, by using different mammalian cell lines, we demonstrate that TOM70, but not TOM20, clusters in distinct OMM foci, frequently overlapping with sites in which the endoplasmic reticulum (ER) contacts mitochondria. Functionally, TOM70 depletion specifically impairs inositol trisphosphates (IP3)-linked ER to mitochondria Ca^{2+} transfer. This phenomenon is dependent on the capacity of TOM70 to interact with IP3-receptors and favor their functional recruitment close to mitochondria. Importantly, the reduced constitutive Ca^{2+} transfer to mitochondria, observed in TOM70-depleted cells, dampens mitochondrial respiration, affects cell bioenergetics, induces autophagy, and inhibits proliferation. Our data reveal a hitherto unexpected role for TOM70 in pro-survival ER-mitochondria communication, reinforcing the view that the ER-mitochondria signaling platform is a key regulator of cell fate.

INTRODUCTION

A large proportion of the outer mitochondrial membrane (OMM) proteome consists of components of the translocase of the outer membrane (TOM). The concerted action of TOM and the mitochondrial translocase of the inner membrane (TIM) is responsible for the post-translational import of nuclear-encoded mitochondrial proteins [1]. TOM is a protein complex consisting of seven subunits. Among them, TOM40 forms dimers and represents

the major structural constituent of the protein-conducting channel, which, together with TOM22 and the small TOM proteins (TOM5, TOM6, and TOM7), constitutes the TOM core complex [2, 3]. In contrast, TOM70 and TOM20 are receptor subunits that are only loosely associated with the TOM core complex [3]. TOM70 and TOM20 interact with each other upon pre-proteins binding, a step that favors their insertion into the TOM channel [4, 5].

Both TOM70 and TOM20 are anchored to the OMM by a N-terminal hydrophobic sequence, while the remaining portion of the proteins is cytosolic [6] and contains tetratricopeptide-repeat (TPR) motifs of large homology. TPRs are essential for protein-protein interactions and recognition of pre-proteins [7]. It has been demonstrated that, after synthesis, several pre-proteins form high-molecular-weight complexes with the cytosolic chaperones Hsp90 and Hsp70. These complexes are docking to TPRs, thus mediating pre-protein targeting to TOM receptors [8]. TOM70 and TOM20 partially differ in their substrate specificity. While TOM20 is mainly involved in the recognition of precursor proteins endowed with cleavable N-terminal pre-sequences, TOM70 binds proteins with internal targeting signals [9]. However, this distinction is mainly quantitative, since the two proteins display overlapping specificities and can substitute one for the lack of the other [6, 10]. Accordingly, cells lacking either TOM70 or TOM20 survive, whereas their simultaneous deletion is lethal [10]. Interestingly, the composition of the TOM complex is dynamic and TOM70/TOM20 transiently associate with the core complex [11]. Specifically, at least half of TOM70 can be retrieved unbound to the complex [10]. This dynamic association raises the possibility that TOM70/TOM20 have partially different distribution within the OMM. In addition, whether the "free" fraction of these proteins may have TIM/TOM complex-independent functions, or simply represent a dormant state of the receptors primed for the binding of pre-proteins, is unknown. Importantly, most of the studies on different TOM subunits have been obtained in yeast. Whether their mammalian homologs exactly conserve the same functions or, during evolution, have acquired new ones remains an outstanding question.

Here, we studied the distribution of TOM70 and TOM20 in mammalian cells. We found that, while TOM20 is present along
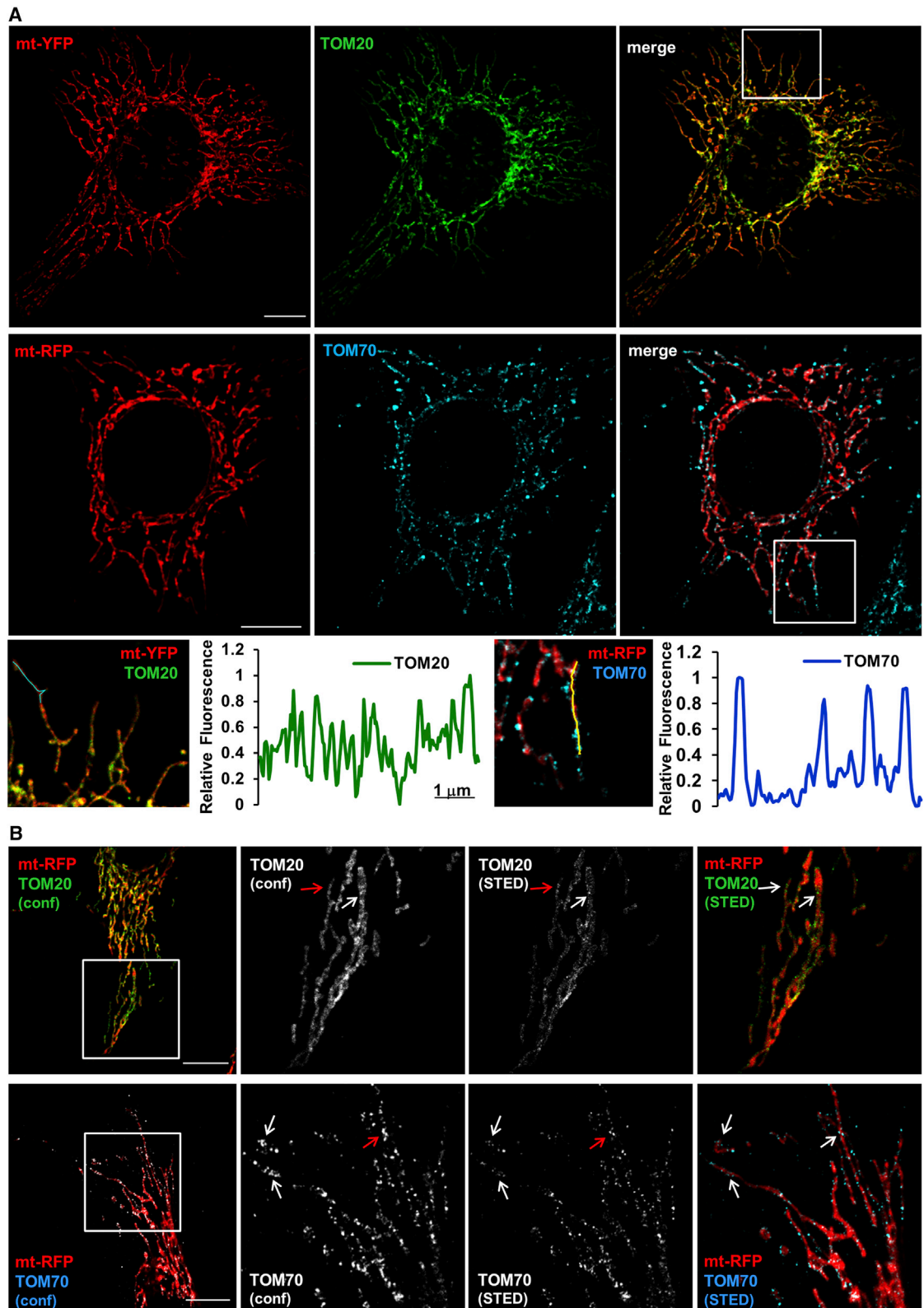
Figure 1. TOM70 Forms Clusters within the Mitochondrial Network

(A) Confocal images of HeLa cells, expressing a mitochondrial matrix targeted YFP (mt-YFP, top) or RFP (mt-RFP, middle panels) and immunostained for endogenous TOM20 (top) or TOM70 (middle). Highlighted boxes (right panels) show regions reported below at higher magnification. Scale bar, 10 μm. In the

the entire mitochondrial network, TOM70 clusters in distinct foci within the OMM. TOM70 puncta are frequently associated with sites in which the endoplasmic reticulum (ER) contacts mitochondria, also referred to as mitochondria-associated membranes (MAM) [12]. While mitochondria morphology and their physical apposition to the ER are conserved, the inositol trisphosphates (IP3)-dependent ER to mitochondria Ca^{2+} transfer is specifically affected in TOM70-depleted cells. Indeed, TOM70 and IP3R3 interact both *in vitro* and in living cells. In cells depleted of TOM70, the reduction of constitutive ER to mitochondria Ca^{2+} shuttling has a dramatic impact on cell bioenergetics, induces autophagy, and affects cell proliferation. Overall, our findings reveal a hitherto unexpected function of TOM70, adding further information to the complex and dynamic nature of ER-mitochondria communication.

RESULTS

TOM70 Clusters at ER-Mitochondria Contact Points

The distribution of endogenous TOM70 and TOM20 within the OMM was investigated by immunofluorescence (IF) in HeLa cells expressing a mitochondria-targeted YFP or RFP. As shown in Figure 1A, the two proteins were not equally distributed along mitochondria; instead, TOM70 tends to cluster in distinct foci while TOM20 staining covered almost the entire mitochondrial network (see the two specific plot line graphs). Similar results were obtained in wild-type (WT) MEFs (Figure S1A), suggesting that the observed distribution is cell type independent. Importantly, the IF signal for TOM70 was specific, since a similar staining was obtained with a different antibody (Figure S1B) and its intensity was substantially dampened by small interfering RNA (siRNA)-mediated protein downregulation (Figures S1C and S1D). Interestingly, a combined plot analysis of double IF images (Figure S1E) shows that, although not enriched, TOM20 was also present within TOM70 foci.

The unexpected distribution of these TOM subunits led us to further investigate the phenomenon. Nano-clusters of TOM20 were previously observed by super-resolution stimulated emission depletion (STED) microscopy in HeLa cells, with a protein gradient from perinuclear to peripheral mitochondria [13]. On the contrary, to the best of our knowledge, no detailed studies on TOM70 sub-mitochondrial distribution in mammalian cells have been published. We thus performed a STED microscopy analysis of HeLa cells expressing a mitochondrial RFP, and in which endogenous TOM70 and TOM20 were labeled by specific antibodies. While TOM20 tended to form nano-domains that decorated almost the entire OMM, TOM70 was retrieved in nano-domains clustered in more distinct and isolated foci (Figures 1B and S1F). Interestingly, a recent proteomic study in yeast identified TOM70 as a critical component of ER-mitochondria

contact sites, where it is enriched and recruits the ER-localized sterol-transporter Ltc1 [14]. We thus tested whether, by following the mitochondrial profiles, TOM70 clusters observed in HeLa cells are associated with the sites of contact between ER and mitochondria. To this end, HeLa cells expressing an ER-CFP and a mitochondrial YFP were immunostained for endogenous TOM70 or TOM20 and subsequently analyzed by confocal microscopy. Our results revealed that, while TOM20 is not selectively enriched at mitochondria-ER contact sites (Figure 2A), TOM70 clusters frequently localized to mitochondrial network regions juxtaposed to the ER (Figure 2B; 63.8% ± 2%, mean ± SEM, n = 220 dots from 5 independent experiments). To further investigate this point, we used a novel, recently characterized split-GFP-based [15] sensor (SPLICS$_L$) for the visualization of ER-mitochondria contacts in living or fixed cells [16]. The probe consists of two non-fluorescent fragments of the split-GFP targeted to the cytosolic face of the ER membranes and the OMM, respectively. The GFP fluorescence will be reconstituted only at the points in which the ER is in close contact (<40–50 nm) with mitochondria (see STAR Methods for details). HeLa cells expressing the SPLICS$_L$ probe and immunostained for endogenous TOM70 or TOM20 were thus analyzed and the fraction of TOM70 and TOM20 positive pixels that co-localize with ER-mitochondria contacts, marked by the reconstituted split-GFP probe, was quantified. As a control, SPLICS$_L$ was co-expressed with a previously described OMM-targeted RFP [17]. In agreement with the results shown in Figures 2A and 2B, TOM70 co-localization with ER-mitochondria contacts was significantly higher as compared to TOM20 and OMM-RFP (Figures 2C and 2D). Last, western blot analysis of mouse brain sub-cellular fractionations revealed that considerable amounts of both TOM70 and TOM20 were retrieved in the MAM enriched fraction, though both proteins were more abundant in the pure mitochondrial fraction (Figure 2E).

TOM70 Downregulation Specifically Impairs IP3-Mediated ER-Mitochondria Ca^{2+} Transfer

Next, we decided to investigate whether TOM70 and TOM20 can also have a functional role at MAM. Several important cellular processes, including mitochondrial Ca^{2+} uptake, are known to deeply depend on the close apposition of ER and mitochondria at MAM [18, 19]. Here, WT MEF cells, expressing different aequorin-based Ca^{2+} probes (located either in the cytosol or in the mitochondrial matrix) and in which TOM70 or TOM20 were acutely knocked down (KD) by specific siRNA (Figure S1D), were tested for mitochondrial Ca^{2+} rises in response to different cell stimulations. MEFs cells were preferentially used in these experiments due to the efficiency of RNAi-based downregulation of TOM70 or TOM20 protein expression. Mitochondrial Ca^{2+} peaks, induced by an IP3-linked ER Ca^{2+} release, were lower

enlarged TOM20/TOM70 merge boxes, a line has been drawn on a branch of the mitochondrial network and the relative fluorescence intensity profiles of the two signals have been plotted (bottom graphs). Note that, while the TOM20 signal intensity is more homogeneously distributed, that of TOM70 shows discrete peaks, corresponding to TOM70 clusters.

(B) Confocal images of HeLa cells, expressing mt-RFP and immunostained for endogenous TOM20 or TOM70. Scale bar, 10 μm. Highlighted boxes (left panels) show regions reported at higher magnification (on the right), in which a comparison between standard confocal (conf) and STED (STED) microscopy acquisition of TOM20 or TOM70 signal was performed. Arrows indicate points in which STED microscopy allows to better appreciate the clustered distribution of the two proteins. Red arrows indicate regions further magnified in Figure S1F. Scale bar, 10 μm.

See also Figure S1.
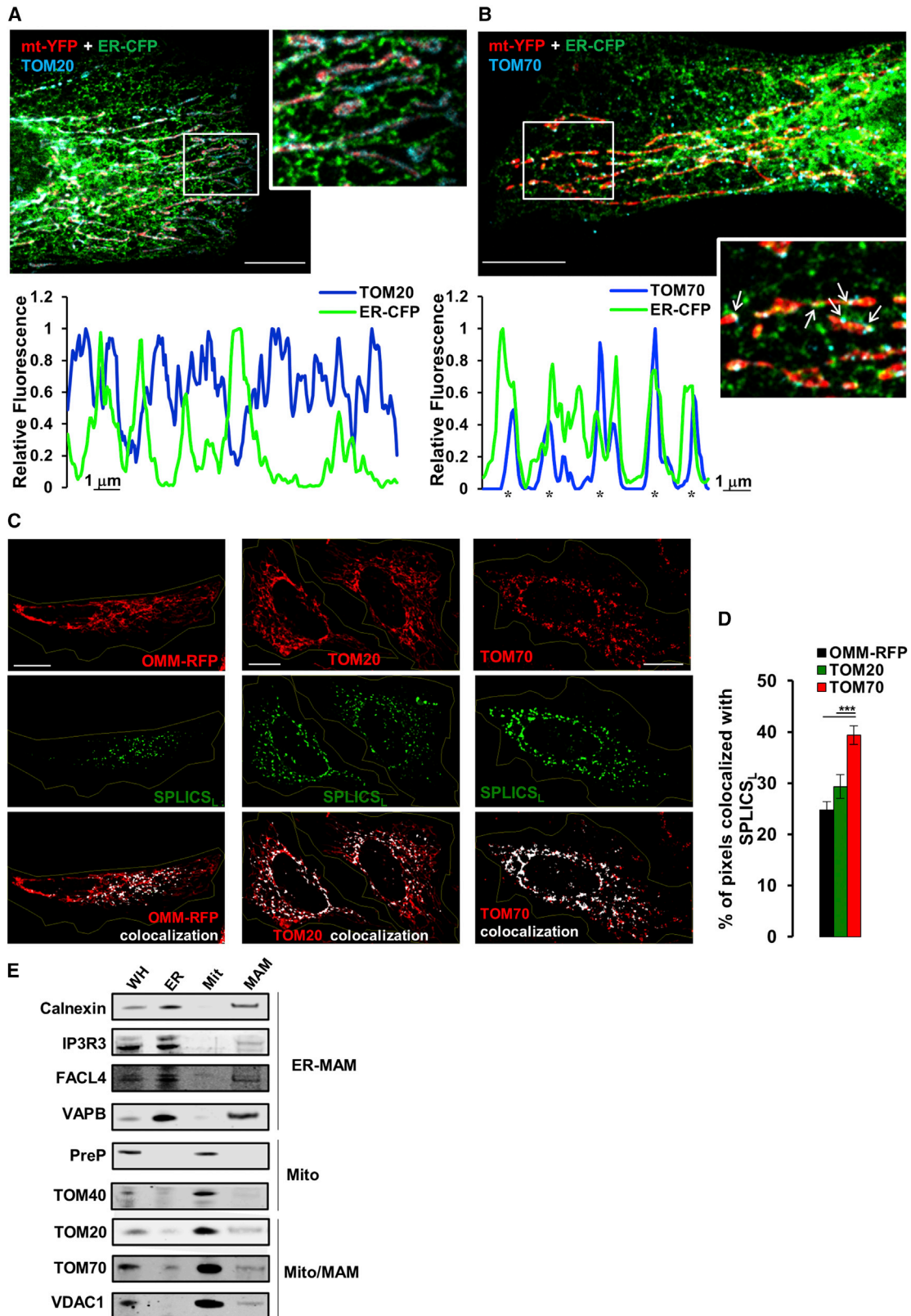
Figure 2. TOM70 Clusters Are Frequently in Contact with the ER

(A and B) Confocal images of HeLa cells expressing mt-YFP and ER-CFP and immunostained for endogenous TOM20 (A) or TOM70 (B). Highlighted boxes show regions at higher magnification. Scale bar, 10 μm. In (B), several TOM70 dots are associated with ER-mitochondria co-localization regions (white arrows). The

(legend continued on next page)

in TOM70-KD, but not in TOM20-KD cells, as compared to controls (Figure 3A). Importantly, cytosolic Ca^{2+} transients, evocated by the same stimulation, were similar in the three conditions (Figure S2A), indicating that the observed reduced mitochondrial Ca^{2+} uptake does not depend on the release of different Ca^{2+} amounts from the ER. Accordingly, ER Ca^{2+} content was not affected by TOM70 depletion, as directly revealed by the ER targeted cameleon Ca^{2+} probe D4ER [20] (Figure S2B). The defective IP3-linked mitochondrial Ca^{2+} uptake induced by TOM70 depletion was recovered by the co-expression of a siRNA-resistant form of the protein (Figure S2D), indicating that the effect is specific.

Mitochondrial Ca^{2+} uptake is favored by the generation of "Ca^{2+} hotspots" on their surface [21] and shaped by the intrinsic capacity of these organelles to take up the cation, through the mitochondrial Ca^{2+} uniporter (MCU) complex [22]. In order to directly evaluate the impact of TOM70 depletion on the latter parameter, the following experiments were performed. Mitochondrial Ca^{2+} rises were measured in control and TOM70-KD cells upon (1) induction of cell Ca^{2+} entry through endogenous plasma membrane (PM) Ca^{2+} channels activated by ER Ca^{2+} depletion (capacitative Ca^{2+} entry, CCE [23]) (Figure S2C) and (2) cell permeabilization and perfusion with different media containing fixed $[Ca^{2+}]$ (2, 5, 10 μM; Figures S2E and S2F). In both cases, no significant differences were observed as compared to controls. Importantly, MCU expression was not affected by TOM70 depletion (Figure S2G; Table S1) and tetramethyl rhodamine methyl ester (TMRM) measurements did not reveal appreciable differences in mitochondrial Δψ (Figure S2H). Overall, the above data suggest that the general capacity of mitochondria to take up Ca^{2+} is not affected by TOM70 depletion and the observed reduction in mitochondrial Ca^{2+} uptake (Figure 3A) is specifically linked to IP3Rs stimulation.

To further assess the role of TOM70 and TOM20 in functionally maintaining the ER-mitochondria Ca^{2+} axis, an aequorin variant targeted to the mitochondrial inter-membrane space (MIMS [19]) was used. By this tool, upon an IP3-dependent ER Ca^{2+} release, it is possible to report averaged Ca^{2+} peaks higher than those occurring in the bulk cytosol (Figure 3B), reflecting the privileged apposition of mitochondria to sites of Ca^{2+} release from the ER [19]. Importantly, the measurement of $[Ca^{2+}]$ in the MIMS, i.e., a step before the uptake of the cation in the mitochondrial matrix through the inner mitochondria membrane (IMM)-located MCU, allows to evaluate more precisely the efficiency of the ER-mitochondria Ca^{2+} transfer, overcoming possible misleading results due to small alterations in mitochondrial Δψ or MCU activity [19]. We found that, upon IP3-dependent ER Ca^{2+} release,

MIMS-Ca^{2+} peaks were dampened in TOM70-KD, but not in TOM20-KD cells (Figure 3B). Notably, CCE-induced MIMS Ca^{2+} rises were not affected by TOM70-KD (Figures 3C and S2C). Again, these data suggest that TOM70 depletion specifically impairs IP3Rs-dependent ER-mitochondria Ca^{2+} coupling.

TOM70 Recruits IP3R3 Close to Mitochondria

The mechanisms through which TOM70-KD affects ER-mitochondria Ca^{2+} shuttling could be multiple. Alterations in the OMM Ca^{2+} permeability are unlikely, because CCE-elicited MIMS-Ca^{2+} rises are unaffected (Figures 3C and S2C). The more obvious explanation for these data is a reduced ER-mitochondria physical apposition upon TOM70-KD, a feature capable of impacting on the efficiency of their Ca^{2+} transfer. Interestingly, the analysis of ER-mitochondria juxtaposition, by confocal and electron microscopy (EM; Figures S3A–S3C), did not reveal significant differences between controls and TOM70-KD cells. EM analysis showed that the number of contacts per mitochondrial profile, as well as the percentage of OMM in contact with ER, were not altered by TOM70 depletion. The generation of Ca^{2+} hot spots on mitochondria surface is, however, modulated not only by organelles apposition with the ER, but also by the specific enrichment at MAM of clusters of functional ER Ca^{2+} releasing channels [24]. IP3Rs can form a macromolecular complex with the mitochondrial protein VDAC1 and the cytosolic fraction of GRP75, favoring the tunneling of IP3Rs-released Ca^{2+} directly into mitochondria [25]. Among the different IP3Rs isoforms, IP3R3 has been reported to be enriched at MAM and preferentially involved in ER to mitochondria Ca^{2+} transfer [26, 27]. We thus investigated whether TOM70 could be important for proper IP3R3 recruitment/stabilization at ER domains close to mitochondria. Control and TOM70-KD MEF cells, expressing a mitochondrial YFP, were immunostained for endogenous IP3R3 (Figure 3D). Confocal microscopy analysis revealed a net decrease in IP3R3 co-localization with mitochondria upon TOM70 depletion (Figure 3D), although the latter treatment slightly increases the total expression level of the protein (Figure S2G; Table S1). These results suggest a possible IP3R3 redistribution within ER membranes upon TOM70 depletion, likely impairing the correct assembly/stability of the IP3R3-GRP75-VDAC1 complex and explaining the reduced ER-mitochondria Ca^{2+} transfer (Figures 3A and 3B). Importantly, in VDAC1 and 3 ($VDAC1/3^{-/-}$) knocked out MEFs, i.e., a cell line in which the formation of the IP3R3-GRP75-VDAC1 complex is not possible, cytosolic, MIMS, and mitochondrial matrix Ca^{2+} peaks induced by IP3-linked stimulations were unaffected upon TOM70 depletion (Figure 3E), further

graphs below (A and B) represent relative fluorescence intensity of ER-CFP and TOM20 (A) or TOM70 (B). Note that, while TOM20 fluorescence peaks do not match with those of ER-CFP (A), TOM70 ones frequently coincide with peaks of ER-CFP fluorescence (indicated by * in B). After acquisition, images were background subtracted and processed as detailed in STAR Methods.

(C) Confocal images of HeLa cells, expressing the ER-mt split-GFP-based sensor (SPLICS_L) and co-expressing an OMM-RFP (left) or immunostained for endogenous TOM20 (middle) or TOM70 (right). In the bottom panels, white pixels indicate co-localization between the two signals. Cell perimeters, traced according to the IF signal of the cytosolic marker lactate dehydrogenase A (LDH-A) (not shown), are drawn (yellow lines). Scale bars, 10 μm.

(D) Bars represent the mean percentage of pixels of the indicated signal co-localized with ER-mt SPLICS_L labeled sites, calculated from images as in (C) (mean ± SEM; n ≥ 32 cells per condition). Scale bar, 10 μm.

(E) Brains from C57B6/J mice were homogenized and sub-fractionated (n = 3). Isolated subcellular fractions were analyzed by SDS-PAGE and western blot. Immunostaining for the indicated marker proteins of PM, ER, mitochondria, and MAM was performed, as well as for TOM20 and TOM70. Calnexin, IP3R3, FACL4, and VAPB were used to check the purity of ER and MAM fractions, PreP and TOM40 to check purity of mitochondria fraction, and VDAC1 to check the purity of mitochondria/MAM fraction.
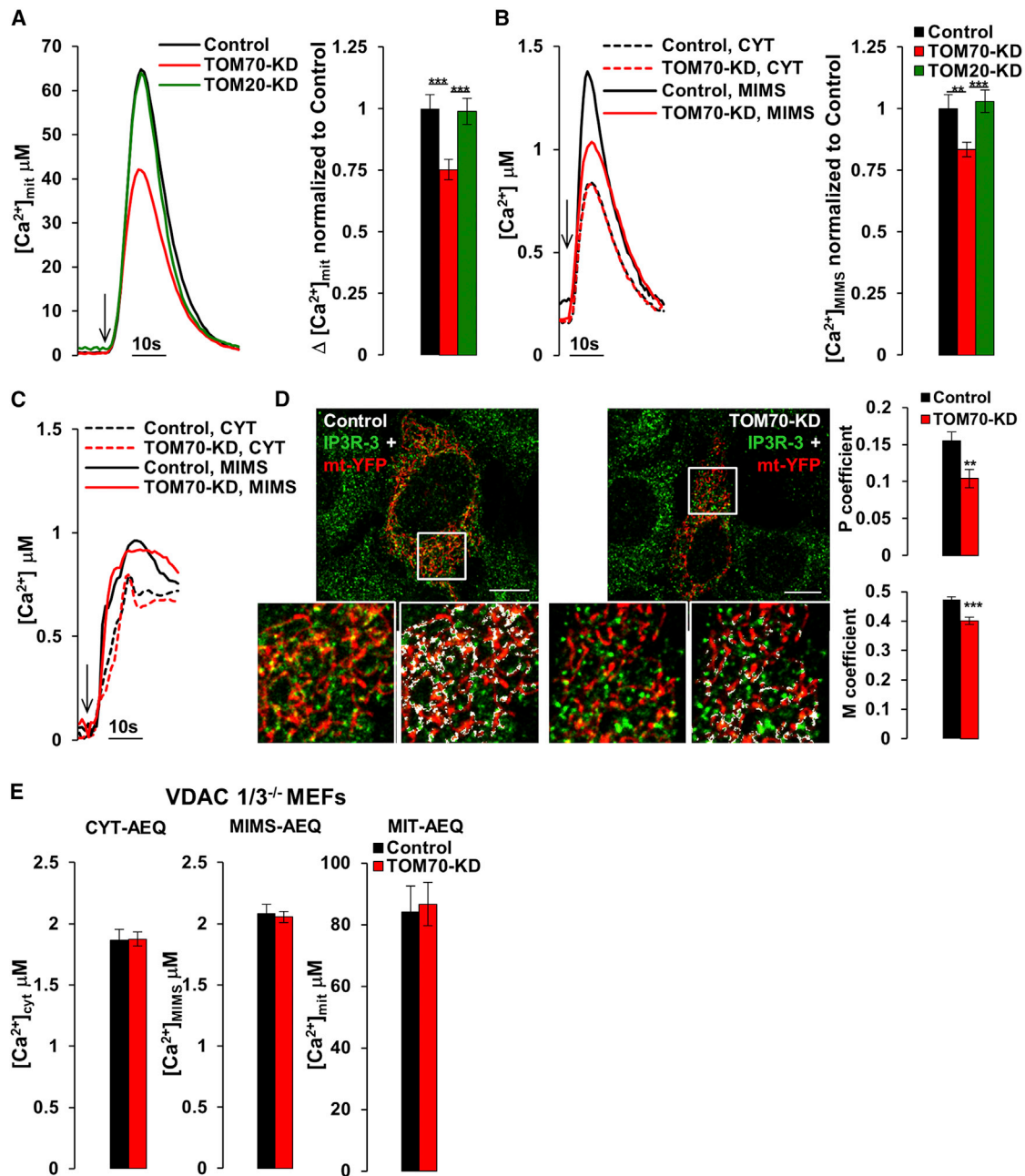
Figure 3. TOM70 Depletion Dampens ER to Mitochondria Ca²⁺ Transfer by Reducing IP3R3 Localization Close to Mitochondria

(A and B) Representative traces and quantifications of mitochondrial matrix (A), cytosolic (dotted traces, B) and MIMS (continuous traces, B) [Ca^{2+}] peaks in WT MEFs, knocked down (KD) for the indicated protein and expressing mitochondrial (A), cytosolic or MIMS aequorin (B). Ca^{2+} transients, obtained after ER-Ca^{2+} release, were elicited by stimulating cells (bathed in a Ca^{2+}-free, EGTA-containing medium) with a mix of IP3-generating agonists (arrows, see STAR Methods). Bars represent mean [Ca^{2+}]$_{mit}$ (A) or [Ca^{2+}]$_{MIMS}$ (B) upon cells stimulation in the indicated conditions (mean ± SEM; n ≥ 7 independent experiments per condition).

(C) Representative traces of cytosolic (dotted traces) and MIMS (continuous traces) [Ca^{2+}] rises obtained after exposure to CaCl₂ (5 mM, arrow) in WT MEFs (CCE, see STAR Methods), expressing cytosolic or MIMS aequorin and transfected with control or TOM70-specific siRNA (TOM-KD).

(D) Confocal images of WT MEFs expressing mt-YFP, transfected with control or TOM70-specific siRNA, and immunostained for endogenous IP3R3. Highlighted boxes show regions at higher magnification, in which IP3R3-mitochondria co-localization is visualized (yellow or white pixels). After acquisition, images were background subtracted and processed as detailed in STAR Methods. On the right, bars represent Pearson's (P) and Manders' (M) coefficients for co-localization between IP3R3 and mitochondria in the indicated conditions (mean ± SEM; n ≥ 36 cells per condition).

(E) Bars represent mean cytosolic, MIMS, and mitochondrial matrix [Ca^{2+}] peaks, obtained stimulating as in (A) and (B) *VDAC1/3⁻/⁻* MEFs, control, or KD for TOM70, and expressing cytosolic, MIMS, or mitochondrial aequorin (mean ± SEM; n ≥ 8 independent experiments per condition).

See also Figures S2 and S3.
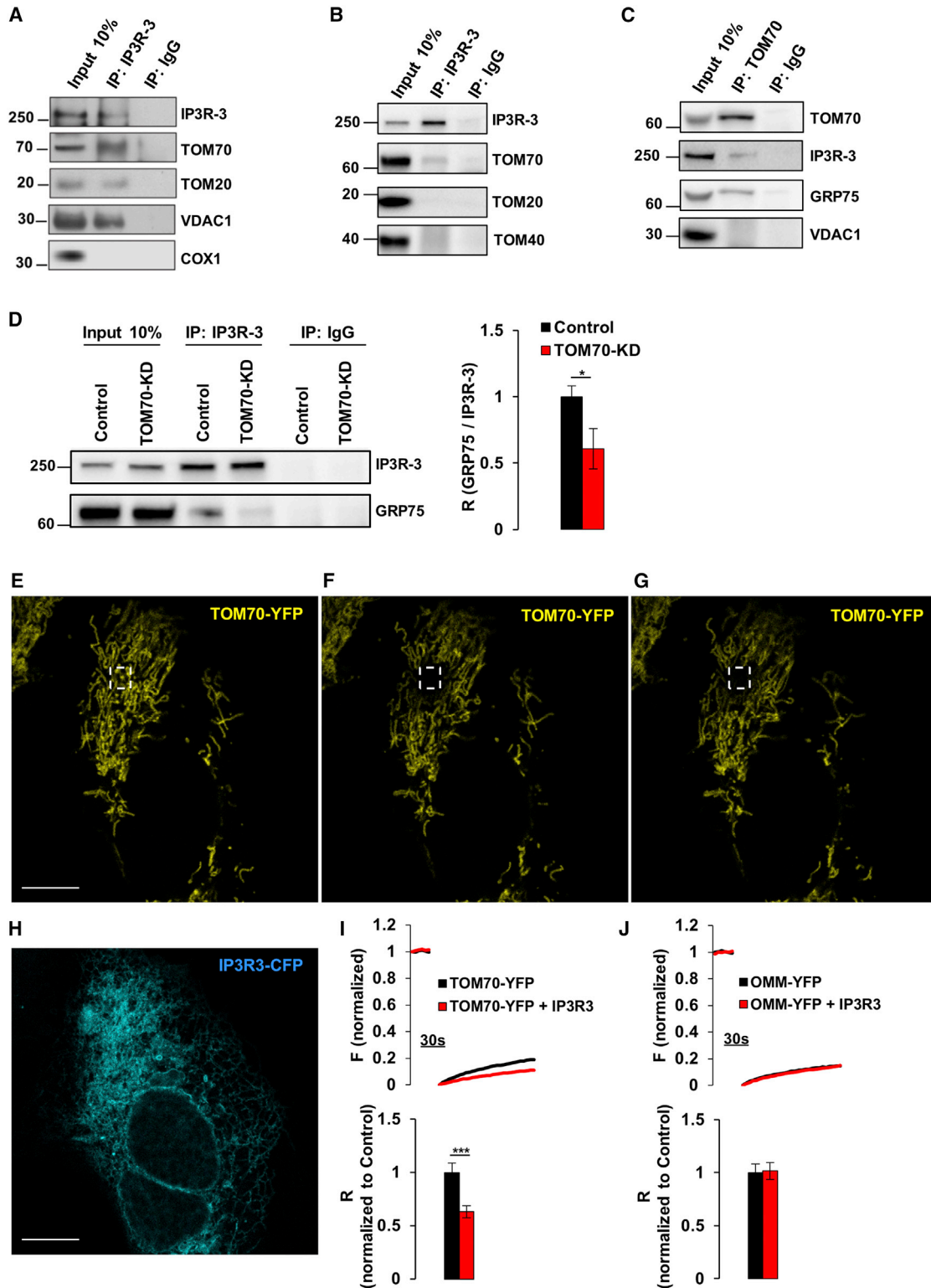
Figure 4. TOM70 Physically Interacts with IP3R3

(A–C) Representative western blot of co-IP experiments (n = 3) performed in crude mitochondrial fractions from brains of C57BL6/J mice (A) or in total homogenate from MEF cells (B and C). IP3R3 (A and B) or TOM70 (C) were precipitated by specific monoclonal antibodies, and the co-precipitated samples were analyzed by SDS-PAGE and probed with the indicated antibodies.

(legend continued on next page)

A

B

Condition	# dots per cell ± SEM
IP3R3 - TOM70	4.5 ± 0.07
IP3R3 - TOM20	9.8 ± 0.15
IP3R3+	25.6 ± 0.50
IP3R3-	0.3 ± 0.02
TOM70+	89.5 ± 1.20
TOM70-	0.8 ± 0.04
TOM20+	228.2 ± 4.10
TOM20-	2.6 ± 0.09

C
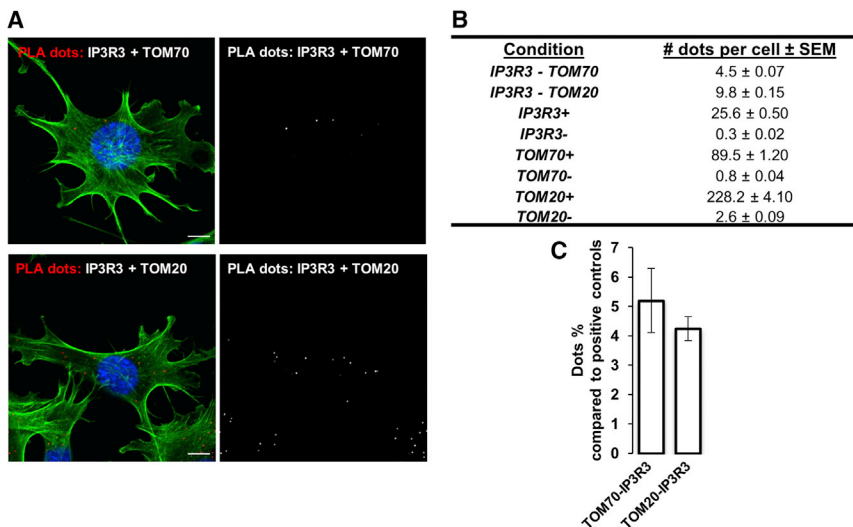
Figure 5. PLA TOM70 and TOM20 Are in Close Proximity to IP3R3

(A) Representative confocal images of WT MEF cells using proximity ligation assay (PLA) between IP3R3 (mouse) and TOM70 (rabbit) or IP3R3 (mouse) and TOM20 (rabbit) couple antibodies. Nuclei were stained with DAPI, F-actin was stained with phalloidin (green), and the PLA amplification reaction is visualized as red dots. Left panels correspond to merged images, right panels correspond to split black and white images of PLA dots. Scale bar, 10 μm.

(B) Quantification of dots (number of dots per cell; mean ± SEM) in PLA couple antibodies, negative and positive controls for each antibody used (see STAR Methods, n ≥ 52 cells from 3 independent experiments).

(C) Bars represent the percentage of dots for the IP3R3-TOM70 couple (or IP3R3-TOM20 couple) compared to those present in respective positive controls (mean ± SEM, n = 3 independent experiments). See also Figure S4.

suggesting that TOM70 impinges on this specific Ca²⁺-handling machinery.

To further investigate the possible mechanism by which TOM70 influences IP3R3 distribution and functionality, we tested whether the two proteins physically interact. Endogenous IP3R3 was pulled down from mouse brain-derived crude mitochondrial fractions, and co-immunoprecipitated proteins were detected by immunostaining of the separated complexes. Our results confirm that the OMM protein VDAC1 can be pulled down with IP3R3 [28] and, importantly, show that TOM70 (and to a lower extent TOM20) also co-immunoprecipitated with IP3R3 (Figure 4A). Similar experiments performed in total homogenate of WT MEFs showed that IP3R3 co-immunoprecipitated with TOM70 (Figure 4B), while a clear band for TOM20 and TOM40 was not observed in the pulled-down fraction. Interestingly, by reverse immunoprecipitation of TOM70, both IP3R3 and GRP75 proteins were pulled down, while VDAC1 was not retrieved in this fraction (Figure 4C). These results suggest that TOM70 interacts with the IP3R3-GRP75 complex. Importantly, when IP3R3 was immunoprecipitated in control and TOM70-KD MEFs, lower amounts of GRP75 were found in the pulled-down fraction of the latter cell type (Figure 4D), suggesting an active role of TOM70 in the formation/stabilization of this Ca²⁺ signaling complex, that may explain the effect of TOM70-KD on the ER to mitochondria Ca²⁺ transfer (Figures 3A and 3B).

TOM70 and IP3R3 interaction was also analyzed in living cells using fluorescence recovery after photobleaching (FRAP [29]). These experiments showed that the mobility of TOM70-YFP

(but not of an OMM-YFP [21]) within the OMM was modulated by the presence of IP3R3. Figures 4E–4G shows representative confocal images of an IP3Rs-KO human embryonic kidney (HEK) cell expressing TOM70-YFP before (Figure 4E) and after (Figures 4F and 4G) photobleaching in a specific region. Representative FRAP traces of IP3Rs-KO HEK cells expressing TOM70-YFP (Figure 4I) or OMM-YFP (Figure 4J), alone or together with IP3R3-CFP (a fluorescent form of the receptor to visualize transfected cells, Figure 4H), are also presented. IP3R3 co-expression (red traces) did not affect fluorescence recovery of OMM-YFP (Figure 4J), while it significantly reduced that of TOM70-YFP (Figure 4I). Accordingly, the mobile fraction (R) of TOM70-YFP (Figure 4I, bottom), but not that of OMM-YFP (Figure 4J, bottom), was reduced by IP3R3 co-expression. Altogether, these findings exclude a possible TOM70 mobility interference due to differential organelle's apposition in the presence or not of the IP3R3, since the mobile fraction of OMM-YFP was not affected. Instead, they strongly suggest that the observed reduction in TOM70 mobile fraction in the presence of IP3R3 is due to their physical interaction that could be either direct or mediated by additional molecules.

In agreement with these results, juxtaposition (<40 nm) between IP3R3 and TOM70 was also demonstrated by proximity ligation assay (PLA; Figure 5). We performed PLA in WT MEF cells, and the analysis showed a clear pattern of apposition between IP3R3 and TOM70, and to a lesser extent between IP3R3 and TOM20 (Figure 5). The PLA signal in positive and negative controls (see STAR Methods) is shown in Figure S4.

(D) Representative western blot of co-IP experiments performed in control or TOM70-KD MEF cells. IP3R3 was precipitated with a specific monoclonal antibody, and the co-precipitated samples were probed for GRP75 and IP3R3. On the right, bars represent the ratio between GRP75 and IP3R3 bands in the corresponding precipitated samples (mean ± SEM; n = 5 independent experiments).

(E–H) Representative confocal images showing an IP3Rs-KO HEK cell co-expressing TOM70-YFP (E–G) and IP3R3-CFP (H) before (E and H) and after (F and G) photobleaching in the drawn region of interest (ROI). Scale bar, 10 μm.

(I and J) On the top, representative FRAP traces of TOM70-YFP (I) or OMM-YFP (J) expressing IP3Rs-KO HEK cells, with (red) or without (black) co-expression of IP3R3-CFP. Traces represent fluorescence intensities in the selected ROI before and after photobleaching for the indicated time. Fluorescence intensity was normalized to that before photobleaching. On the bottom, bars represented mean values of the mobile fraction (R) of TOM70-YFP (I) or OMM-YFP (J) in the presence (red) or absence (black) of IP3R3 (mean ± SEM; n ≥ 23 cells per condition).
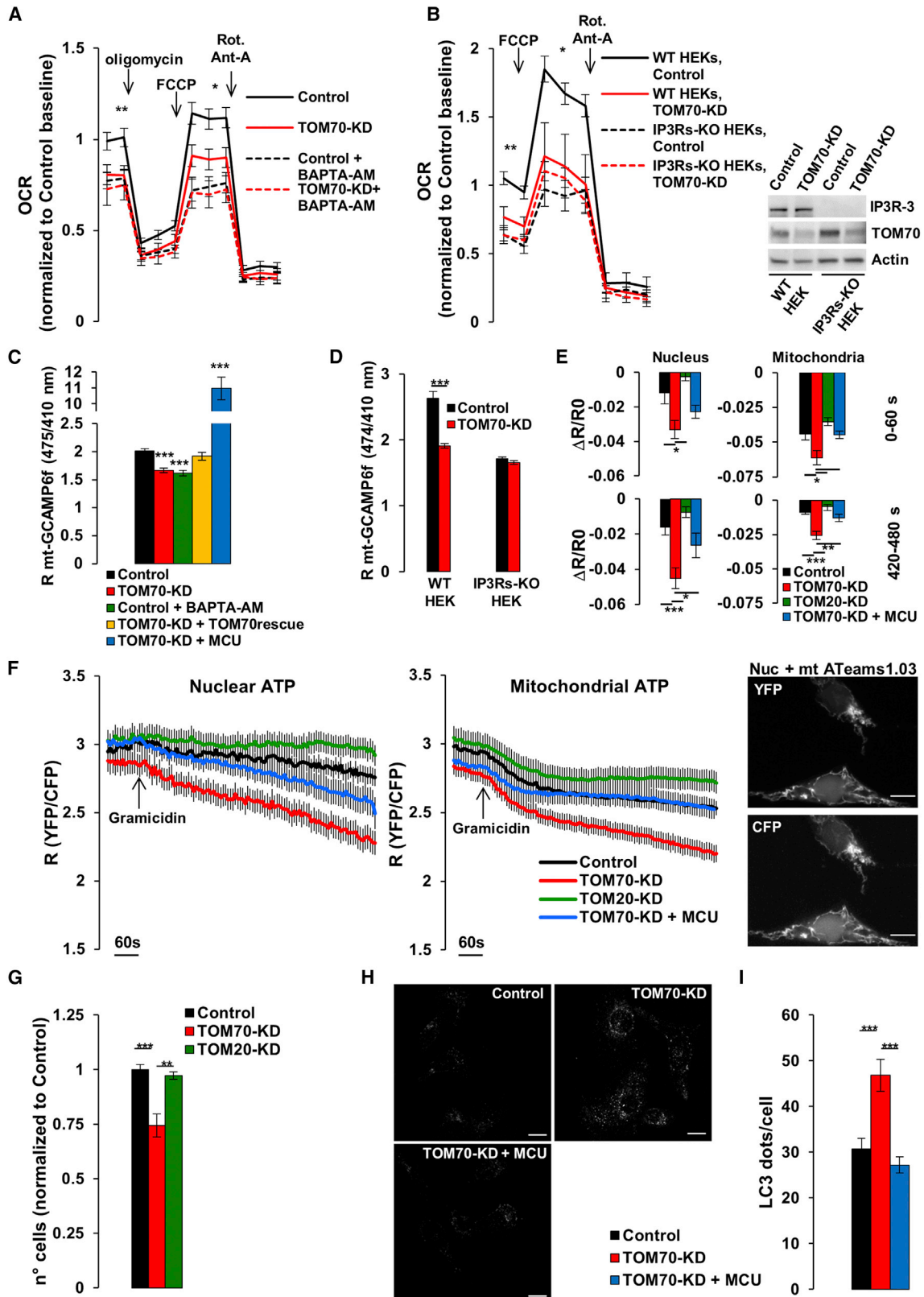
(legend on next page)

TOM70-Downregulation Impairs Cell Bioenergetics by Affecting ER-Mitochondria Ca^{2+} Transfer

The constitutive ER-mitochondria Ca^{2+} transfer has been demonstrated to be important for mitochondrial functions regulation. In particular, basal IP3Rs activity and continuous, low-level Ca^{2+} flux from ER to mitochondria is essential to promote mitochondrial respiration and cell bioenergetics, by sustaining the Krebs' cycle through regulation of three Ca^{2+}-modulated dehydrogenases [30]. In order to elucidate whether the TOM70-KD-dependent impairment in ER-mitochondria Ca^{2+} transfer also impacts mitochondrial functions and cell metabolism, mitochondrial respiration was measured (by Seahorse analysis) in control and TOM70-KD MEF cells. Fetal calf serum (FCS) was included in the experimental buffer (see STAR Methods) as a mix of different stimuli that promotes constitutive IP3Rs activity, as previously shown [30]. Both basal and maximal respiration were decreased upon TOM70 depletion (Figure 6A). Importantly, the effect was specifically due to impairment in mitochondrial Ca^{2+} uptake and not to intrinsic defects of the respiratory chain. Indeed, the drop in respiration was blunted in cells pre-treated with 1,2-Bis(2-aminophenoxy)ethane-N,N,N0,N0-tetraacetic acid tetrakis(acetoxymethyl ester) (BAPTA-AM), a compound capable of buffering intracellular Ca^{2+} hotspots, thus dampening ER-mitochondria Ca^{2+} shuttling (Figure 6A). Moreover, mitochondrial respiration defects were rescued in TOM70-KD MEF cells overexpressing MCU (Figure S5A), as well as in TOM70-KD MEFs co-expressing a siRNA-resistant form of the protein (Figure S5A), suggesting a specific action of TOM70 in the bioenergetics pathway. Importantly, the observed TOM70-KD effect on mitochondrial respiration was strictly IP3Rs dependent and not due to defective mitochondrial proteins import (see below). In fact, TOM70 depletion was effectless on mitochondrial respiration in HEK cells KO for IP3Rs, while in WT HEK cells it induced similar dysfunctions to those observed in MEFs (Figure 6B). Accordingly, when we measured basal mitochondrial [Ca^{2+}], by employing the mitochondrial matrix targeted Ca^{2+} probe GCAMP6f (used in a "ratiometric" manner by exploiting its isosbestic point; see [31] and STAR Methods), we found lower Ca^{2+} levels, as compared to controls, in TOM70-KD and BABTA-AM-treated MEFs (Figure 6C), as well as in TOM70-KD WT HEK cells (Figure 6D, left). No such effect was detected in IP3Rs-KO HEK cells depleted of TOM70 (Figure 6D, right). The signal of the mitochondrial Ca^{2+} sensor was increased in TOM70-KD MEF cells overexpressing MCU (Figure 6C). Consistently with a lower mitochondrial matrix [Ca^{2+}] and a reduced Krebs' cycle activity, TOM70 depletion, but not that of TOM20, also increased Ca^{2+}-modulated phosphorylation of the mitochondrial enzyme pyruvate-dehydrogenase (PDH) (Figure S5B).

Further experiments suggested that the dysfunctional mitochondrial respiration induced by TOM70-KD is not dependent on impairment of mitochondrial protein import. Indeed, both basal and ADP-stimulated oxygen consumption rate (OCR) were similar in permeabilized control and TOM70-KD MEF cells (Figure S5C). Moreover, the expression levels of the mitochondrial pyruvate carrier (MPC1; Figure S5D), as well as the expression (tested in the crude mitochondrial fraction) of the ADP/ATP carrier (ANT; Figure S5D) were not affected by TOM70-KD. Importantly, this latter carrier has been reported to be a classical TOM70 substrate [28]. The partial TOM70 silencing we obtained by our siRNAs may thus not substantially affect the mitochondrial protein import mechanism. We also investigated whether TOM70 depletion alters mitochondrial mass, a feature that can affect respiration. Interestingly, no significant changes in the relative amount of the respiratory chain's protein COXIV were observed, neither in those of the mitochondrial proteins MCU and VDAC1 (Figure S2G; Table S1).

Since a defective mitochondrial respiration can affect ATP production, cellular ATP levels were investigated. By co-expressing previously reported nuclear and mitochondrial fluorescence resonance energy transfer (FRET)-based ATP probes [32], we were able to monitor ATP levels in the two compartments at the same time and in the very same cells (Figure S5E). [ATP] within the nucleus has been shown to be in equilibrium with the cytosolic one, and thus the nuclear compartment can be used as a surrogate of the cytosol [32]. Importantly, given that immortalized cell lines (such as MEFs used in this study) tend

---

Figure 6. TOM70 Depletion Affects Cell Bioenergetics

(A) Oxygen consumption rate (OCR) in WT MEFs, transfected with control or TOM70-specific siRNA (TOM70-KD) and pre-incubated (or not) with BAPTA-AM (5 μM; see STAR Methods). Oligomycin (1 μg/mL), FCCP (1.2 μM), and Rotenone/Antimycin-A (1 μM each) were added where indicated (mean ± SEM; n ≥ 12 independent experiments per condition).

(B) Oxygen consumption rate (OCR) in WT or IP3Rs-KO HEK cells, transfected with control or TOM70-specific siRNA (TOM70-KD) (see the corresponding western blot on the right) and sequentially treated with FCCP (0.25 μM) and Rotenone/Antimycin-A (1 μM each) (mean ± SEM; n ≥ 10 independent experiments per condition).

(C and D) For the indicated conditions in WT MEFs (C), WT, or IP3Rs-KO HEK cells (D), bars represent the mean ratio (R) between emission fluorescence intensities (500–535 nm) of the mitochondrial matrix targeted GCAMP6f probe by sequential excitation at 475 nm (where the absorbance is Ca^{2+} dependent) and at 410 nm (the isosbestic point, where the absorbance is not affected by [Ca^{2+}]) (mean ± SEM; n ≥ 106 cells per condition).

(E) Bars represent the decay rate of the FRET ratio (R, expressed as YFP/CFP ratio) of the nuclear (left) or the mitochondrial (right) ATP probes (ATeams1.03) in WT MEFs transfected as indicated, in the 1st (0–60 s, top) or 8th min (420–480 s, bottom) after gramicidin addition, calculated from FRET traces as in (F) (mean ± SEM; n ≥ 42 cells per condition).

(F) Averaged traces of nuclear (left) and mitochondrial matrix (right) ATP measurements (expressed as YFP/CFP ratio, R) in WT MEFs, co-expressing nuclear and mitochondrial ATP FRET-based probes (ATeams1.03) and co-transfected as indicated (mean ± SEM; n ≥ 42 cells per condition). Arrows indicate gramicidin addition (1 μM). On the right, representative images of YFP and CFP signals obtained from WT MEFs, co-expressing the nuclear and the mitochondrial ATeam1.03. Scale bar, 10 μm.

(G) WT MEFs, control, or KD for the indicated protein were grown in galactose-containing medium and counted 72 hr after transfection (see STAR Methods) (mean ± SEM; n = 4 independent experiments).

(H) Representative confocal images of WT MEFs, transfected as indicated and immunostained for endogenous LC3. Scale bar, 10 μm.

(I) Bars represent the mean number of LC3 dots/cell in the indicated conditions (mean ± SEM; n ≥ 42 cells per condition).

See also Figure S5 and Table S1.

to upregulate glycolysis, and deeply rely on this pathway for ATP production compared to mitochondrial respiration, we used galactose instead of glucose in the culture medium. This treatment forces cells to use the mitochondrial pathway to produce ATP [33]. Unexpectedly, neither nuclear nor mitochondrial basal [ATP] was significantly different in TOM70-KD cells as compared to controls (Figure S5E). However, we reasoned that steady state [ATP] is the result of a balance between ATP production and ATP consumption. Thus, TOM70-KD cells could have dampened some of their energy-consuming metabolic activities, in order to compensate for a lower capacity of their mitochondria to produce ATP. To check this possibility, we challenged cells to consume ATP, by exposing them to a low concentration of gramicidin. Gramicidin is an ionophore capable to insert in the PM and collapse the K^+/Na^+ gradient across it, thus forcing the activity of the Na^+/K^+ ATPase and, consequently, cellular ATP consumption [34]. The prediction is that, if mitochondrial capacity to supply cells with ATP is impaired, the drop in [ATP] within cells should be faster. As shown in Figures 6E and 6F, after gramicidin exposure, [ATP] decreased faster in cells depleted of TOM70 (both in the nucleus and in the mitochondrial matrix; Figure 6E), but not of TOM20, consistently with the observed lower mitochondrial respiration found in the former cell type (Figure 6A). Importantly, overexpression of MCU in TOM70-KD cells, which increases mitochondrial Ca^{2+} uptake and thus rescues their defective matrix [Ca^{2+}] (Figures 6C and S5F), recovered the rate of ATP drop upon gramicidin treatment (Figures 6E and 6F).

In accordance with OCR results (Figure 6A), cell viability was reduced in TOM70-depleted cells grown in galactose-containing medium, as shown by multiple assays (Figure S3D), linking the TOM70-KD-dependent mitochondrial activity alteration with cell death.

It has been recently demonstrated that, in highly proliferating cell lines (such as cancerous cells), mitochondrial activity is not only important for ATP generation, but also for supplying other intermediate metabolites (such as those generated by the Krebs' cycle), that are essential for anabolic metabolism and cells proliferation [35, 36]. The proliferation rate of control and TOM70- or TOM20-KD MEFs, grown in galactose containing medium, was thus evaluated: 72 hr after transfection, we observed a decreased number of TOM70-KD, but not of TOM20-KD cells as compared to controls (Figure 6G).

Last, we investigated the role of TOM70 on the induction of autophagy. Indeed, a previous study reported that impaired cellular bioenergetics, mediated by dysfunctional IP3Rs-induced mitochondrial Ca^{2+} uptake, results in a potent induction of autophagy [30]. Likewise, in our experimental paradigm more LC3 dots (representing autophagosomes) were found in TOM70-depleted cells (Figures 6H and 6I). Notably, the observed increase in autophagosomes reflects a higher rate of autophagy, and not alterations in the autophagy flux. In fact, TOM70-KD cells displayed, compared to controls, a higher number of LC3 dots even after treatment with Bafilomycin A1 (BafA; Figure S5G), an inhibitor of the V-ATPase H^+ pump that blocks autophagolysosomes content degradation by neutralizing pH [37]. Importantly, the increased number of LC3 dots present at fed conditions in TOM70-KD cells was rescued by MCU overexpression (Figures 6H and 6I), confirming that the upregulated autophagy observed in TOM70-KD cells specifically depends on a reduced Ca^{2+} transfer to mitochondria.

DISCUSSION

Our data reveal a novel unexpected function for TOM70 in sustaining cells bioenergetics, by promoting IP3Rs-dependent Ca^{2+} transfer from ER to mitochondria. This mechanism does not depend on mitochondrial network alterations or its physical juxtaposition with the ER, nor on modulation of the ER Ca^{2+} content/release or the intrinsic capacity of mitochondria to take up Ca^{2+}. Specifically, TOM70 preferentially resides in clusters frequently associated with ER-mitochondria contact sites, interacts with IP3R3, and favors its enrichment close to mitochondria, promoting Ca^{2+} shuttling to these organelles likely through the IP3R-GRP75-VDAC1 complex. This, in turn, promotes Krebs' cycle and sustains mitochondrial respiration.

Our finding that TOM70 is frequently associated with ER-mitochondria contacts is supported by a proteomic study, in which different components of the TOM complex have been detected in the MAM fraction obtained from mouse brains [38]. Moreover, very recently, a novel approach, using proximity biotinylation and mass-spectrometry identification of potential MAM proteins, retrieved TOM70 as one of the major proteins specifically enriched in ER-mitochondria contacts (the third protein in a score list [39]). Additionally, in yeast, components of the extracellular matrix (ECM) complex, which tethers ER and mitochondria, have been shown to interact with the TOM subunit TOM5 [40]. More recently, TOM70/71 has been found to be highly enriched at ER-mitochondria contacts, where it recruits the sterol transporter Ltc1 [14]. Whether TOM70 is also involved in ER-mitochondria lipids transfer in mammals is unknown. However, the TOM70-IP3R3 Ca^{2+}-relationship described in the present study appears to be a specialized function acquired by TOM70 in higher organisms. Indeed, neither IP3Rs nor MCU homologs have been identified in yeast.

The precise molecular definition of the TOM70-IP3R3 interplay will require further research, since additional proteins could take part in it. Indeed, the functional IP3R3 partner GRP75 was also found to co-immunoprecipitate with TOM70, and, interestingly, TOM70-KD affects IP3R3-GRP75 interaction. Although TOM20 and TOM70 share multiple features within the cell, the finding that TOM20 depletion is effectless on ER-mitochondria Ca^{2+} transfer indicates that, in this signaling pathway, a specific cooperation between IP3R3 and TOM70 occurs. Moreover, we observed that IP3R3 expression levels are slightly increased in TOM70-KD cells (Figure S2G; Table S1), suggesting the possibility that the two proteins are reciprocally regulated. Finally, TOM70 interacts with the cytosolic chaperone Hsp90 [8], which, in turn, has been shown to bind and modulate the activity of the IP3R3 [41], reinforcing the idea that other proteins may be involved in the functional co-ordination of the TOM70/IP3R3 complex.

Regarding the role of TOM70 within the TIM/TOM complex, our data imply that a subpopulation of TOM complexes may reside in close proximity to "Ca^{2+} hotspots" generated at MAM [21, 25, 42]. In fact, TOM70 and TOM20 contain TPR repeats, essential in recognition of pre-proteins [5, 9], which have been shown to establish Ca^{2+}-sensitive protein-protein interactions [43]. Recent evidence suggests that mitochondrial

protein import may be also Ca^{2+} regulated [44]. TOM70 presence at ER-mitochondria contacts, subcellular regions characterized by high and rapid fluctuations in Ca^{2+} concentration, suggests that mitochondrial protein import might be modulated by this Ca^{2+}-based signaling pathway. This implies that the close apposition of TOM70 to the Ca^{2+} releasing channel IP3R3 may open up new perspectives for future research. However, the effects of TOM70-KD reported here are likely not due to an impairment in pre-protein translocation. Indeed, TOM20 and TOM70 can partially compensate one another in this function [10]. Moreover, the two receptors cooperate in the import activity, which is equally reduced by TOM20 ablation [10]. Thus, the fact that ER-mitochondria Ca^{2+} transfer is affected by TOM70-KD alone suggests that translocation activity is not involved. Finally, in our KD experiments, TOM70 levels decrease by ∼60% (Figure S1D; Table S1), allowing a residual import activity, as suggested also by the fact that we did not observe any mis-targeting of different mitochondrial probes, nor defective ANT insertion within mitochondria (Figure S5C). Moreover, expression levels of different endogenous mitochondrial proteins, e.g., MCU, COX-IV and VDAC1 were not decreased after TOM70-KD, further supporting that the process is not significantly altered.

Recent observations that cancer cells strongly rely on Ca^{2+}-stimulated mitochondrial metabolism to exert their anabolic activity [35, 45] imply that the TOM70-IP3R3 complex may be particularly relevant in this process. Interestingly, TOM70 is upregulated in breast cancer [46], as well as IP3Rs [47], and, in ovarian cancer cells, TOM70 and TOM20 levels correlate with insensitivity to iron-induced cell death [48]. In conclusion, the discovery that TOM70 depletion affects cell bioenergetics suggests that the modulation of TOM70 expression or activity could be promising pharmacological targets worth of further investigation in a wide range of pathologies.

STAR★METHODS

Detailed methods are provided in the online version of this paper and include the following:

- KEY RESOURCES TABLE
- CONTACT FOR REAGENT AND RESOURCE SHARING
- EXPERIMENTAL MODEL AND SUBJECT DETAILS
  - Animal models
  - Cell lines
- METHOD DETAILS
  - Aequorin and GCAMP Ca^{2+} measurements
  - Oxygen consumption rate
  - Mitochondrial Transmembrane Potential Measurements
  - ATP and ER-Ca^{2+} FRET measurements
  - Transmission electron microscopy
  - Cell viability
  - Subcellular fractionation of mouse brains
  - Proximity ligation assay (PLA)
  - Co-immunoprecipitation
  - Western blot and immunostaining
  - Immunofluorescence (IF), confocal and STED microscopy, FRAP
- QUANTIFICATION AND STATISTICAL ANALYSIS

REFERENCES

1. Chacinska, A., Koehler, C.M., Milenkovic, D., Lithgow, T., and Pfanner, N. (2009). Importing mitochondrial proteins: Machineries and mechanisms. Cell 138, 628–644.

2. Ahting, U., Thun, C., Hegerl, R., Typke, D., Nargang, F.E., Neupert, W., and Nussberger, S. (1999). The TOM core complex: The general protein import pore of the outer membrane of mitochondria. J. Cell Biol. 147, 959–968.

3. Rapaport, D. (2002). Biogenesis of the mitochondrial TOM complex. Trends Biochem. Sci. 27, 191–197.

4. Brix, J., Dietmeier, K., and Pfanner, N. (1997). Differential recognition of preproteins by the purified cytosolic domains of the mitochondrial import receptors Tom20, Tom22, and Tom70. J. Biol. Chem. 272, 20730–20735.

5. Fan, A.C., Kozlov, G., Hoegl, A., Marcellus, R.C., Wong, M.J., Gehring, K., and Young, J.C. (2011). Interaction between the human mitochondrial import receptors Tom20 and Tom70 in vitro suggests a chaperone displacement mechanism. J. Biol. Chem. 286, 32208–32219.

6. Kulawiak, B., Höpker, J., Gebert, M., Guiard, B., Wiedemann, N., and Gebert, N. (2013). The mitochondrial protein import machinery has multiple connections to the respiratory chain. Biochim. Biophys. Acta 1827, 612–626.

7. Grove, T.Z., Cortajarena, A.L., and Regan, L. (2008). Ligand binding by repeat proteins: Natural and designed. Curr. Opin. Struct. Biol. *18*, 507–515.

8. Young, J.C., Hoogenraad, N.J., and Hartl, F.U. (2003). Molecular chaperones Hsp90 and Hsp70 deliver preproteins to the mitochondrial import receptor Tom70. Cell *112*, 41–50.

9. Truscott, K.N., Brandner, K., and Pfanner, N. (2003). Mechanisms of protein import into mitochondria. Curr. Biol. *13*, R326–R337.

10. Hartl, F.U. (1996). Protein targeting to mitochondria, First Edition (London: Elsevier Science), *17*.

11. Hönlinger, A., Bömer, U., Alconada, A., Eckerskorn, C., Lottspeich, F., Dietmeier, K., and Pfanner, N. (1996). Tom7 modulates the dynamics of the mitochondrial outer membrane translocase and plays a pathway-related role in protein import. EMBO J. *15*, 2125–2137.

12. Vance, J.E. (1990). Phospholipid synthesis in a membrane fraction associated with mitochondria. J. Biol. Chem. *265*, 7248–7256.

13. Wurm, C.A., Neumann, D., Lauterbach, M.A., Harke, B., Egner, A., Hell, S.W., and Jakobs, S. (2011). Nanoscale distribution of mitochondrial import receptor Tom20 is adjusted to cellular conditions and exhibits an inner-cellular gradient. Proc. Natl. Acad. Sci. USA *108*, 13546–13551.

14. Murley, A., Sarsam, R.D., Toulmay, A., Yamada, J., Prinz, W.A., and Nunnari, J. (2015). Ltc1 is an ER-localized sterol transporter and a component of ER-mitochondria and ER-vacuole contacts. J. Cell Biol. *209*, 539–548.

15. Cabantous, S., Terwilliger, T.C., and Waldo, G.S. (2005). Protein tagging and detection with engineered self-assembling fragments of green fluorescent protein. Nat. Biotechnol. *23*, 102–107.

16. Cieri, D., Vicario, M., Giacomello, M., Vallese, F., Filadi, R., Wagner, T., Pozzan, T., Pizzo, P., Scorrano, L., Brini, M., and Cali, T. (2017). SPLICS: a split green fluorescent protein-based contact site sensor for narrow and wide heterotypic organelle juxtaposition. Cell Death & Differentiation. Published online December 11, 2017. https://doi.org/10.1038/s41418-017-0033-z.

17. Csordás, G., Renken, C., Várnai, P., Walter, L., Weaver, D., Buttle, K.F., Balla, T., Mannella, C.A., and Hajnóczky, G. (2006). Structural and functional features and significance of the physical linkage between ER and mitochondria. J. Cell Biol. *174*, 915–921.

18. Csordás, G., Thomas, A.P., and Hajnóczky, G. (1999). Quasi-synaptic calcium signal transmission between endoplasmic reticulum and mitochondria. EMBO J. *18*, 96–108.

19. Rizzuto, R., Pinton, P., Carrington, W., Fay, F.S., Fogarty, K.E., Lifshitz, L.M., Tuft, R.A., and Pozzan, T. (1998). Close contacts with the endoplasmic reticulum as determinants of mitochondrial Ca2+ responses. Science *280*, 1763–1766.

20. Greotti, E., Wong, A., Pozzan, T., Pendin, D., and Pizzo, P. (2016). Characterization of the ER-targeted low affinity Ca(2+) probe D4ER. Sensors (Basel) *16*. Published online September 2, 2016. https://doi.org/10.3390/s16091419.

21. Giacomello, M., Drago, I., Bortolozzi, M., Scorzeto, M., Gianelle, A., Pizzo, P., and Pozzan, T. (2010). Ca2+ hot spots on the mitochondrial surface are generated by Ca2+ mobilization from stores, but not by activation of store-operated Ca2+ channels. Mol. Cell *38*, 280–290.

22. De Stefani, D., Rizzuto, R., and Pozzan, T. (2016). Enjoy the trip: Calcium in mitochondria back and forth. Annu. Rev. Biochem. *85*, 161–192.

23. Putney, J.W. (2009). Capacitative calcium entry: From concept to molecules. Immunol. Rev. *231*, 10–22.

24. Filadi, R., and Pozzan, T. (2015). Generation and functions of second messengers microdomains. Cell Calcium *58*, 405–414.

25. Szabadkai, G., Bianchi, K., Várnai, P., De Stefani, D., Wieckowski, M.R., Cavagna, D., Nagy, A.I., Balla, T., and Rizzuto, R. (2006). Chaperone-mediated coupling of endoplasmic reticulum and mitochondrial Ca2+ channels. J. Cell Biol. *175*, 901–911.

26. Mendes, C.C., Gomes, D.A., Thompson, M., Souto, N.C., Goes, T.S., Goes, A.M., Rodrigues, M.A., Gomez, M.V., Nathanson, M.H., and Leite, M.F. (2005). The type III inositol 1,4,5-trisphosphate receptor preferentially transmits apoptotic Ca2+ signals into mitochondria. J. Biol. Chem. *280*, 40892–40900.

27. Hayashi, T., and Su, T.P. (2007). Sigma-1 receptor chaperones at the ER-mitochondrion interface regulate Ca(2+) signaling and cell survival. Cell *131*, 596–610.

28. Ryan, M.T., Müller, H., and Pfanner, N. (1999). Functional staging of ADP/ATP carrier translocation across the outer mitochondrial membrane. J. Biol. Chem. *274*, 20619–20627.

29. Reits, E.A., and Neefjes, J.J. (2001). From fixed to FRAP: Measuring protein mobility and activity in living cells. Nat. Cell Biol. *3*, E145–E147.

30. Cárdenas, C., Miller, R.A., Smith, I., Bui, T., Molgó, J., Müller, M., Vais, H., Cheung, K.H., Yang, J., Parker, I., et al. (2010). Essential regulation of cell bioenergetics by constitutive InsP3 receptor Ca2+ transfer to mitochondria. Cell *142*, 270–283.

31. Patron, M., Checchetto, V., Raffaello, A., Teardo, E., Vecellio Reane, D., Mantoan, M., Granatiero, V., Szabò, I., De Stefani, D., and Rizzuto, R. (2014). MICU1 and MICU2 finely tune the mitochondrial Ca2+ uniporter by exerting opposite effects on MCU activity. Mol. Cell *53*, 726–737.

32. Imamura, H., Nhat, K.P., Togawa, H., Saito, K., Iino, R., Kato-Yamada, Y., Nagai, T., and Noji, H. (2009). Visualization of ATP levels inside single living cells with fluorescence resonance energy transfer-based genetically encoded indicators. Proc. Natl. Acad. Sci. USA *106*, 15651–15656.

33. Marroquin, L.D., Hynes, J., Dykens, J.A., Jamieson, J.D., and Will, Y. (2007). Circumventing the Crabtree effect: Replacing media glucose with galactose increases susceptibility of HepG2 cells to mitochondrial toxicants. Toxicol. Sci. *97*, 539–547.

34. Brand, M.D., and Nicholls, D.G. (2011). Assessing mitochondrial dysfunction in cells. Biochem. J. *435*, 297–312.

35. Cárdenas, C., Müller, M., McNeal, A., Lovy, A., Jaňa, F., Bustos, G., Urra, F., Smith, N., Molgó, J., Diehl, J.A., et al. (2016). Selective vulnerability of cancer cells by inhibition of Ca(2+) transfer from endoplasmic reticulum to mitochondria. Cell Rep. *14*, 2313–2324.

36. Porporato, P.E., Payen, V.L., Pérez-Escuredo, J., De Saedeleer, C.J., Danhier, P., Copetti, T., Dhup, S., Tardy, M., Vazeille, T., Bouzin, C., et al. (2014). A mitochondrial switch promotes tumor metastasis. Cell Rep. *8*, 754–766.

37. Mauvezin, C., Nagy, P., Juhász, G., and Neufeld, T.P. (2015). Autophagosome-lysosome fusion is independent of V-ATPase-mediated acidification. Nat. Commun. *6*, 7007.

38. Poston, C.N., Krishnan, S.C., and Bazemore-Walker, C.R. (2013). In-depth proteomic analysis of mammalian mitochondria-associated membranes (MAM). J. Proteomics *79*, 219–230.

39. Hung, V., Lam, S.S., Udeshi, N.D., Svinkina, T., Guzman, G., Mootha, V.K., Carr, S.A., and Ting, A.Y. (2017). Proteomic mapping of cytosol-facing outer mitochondrial and ER membranes in living human cells by proximity biotinylation. eLife *6*. Published online April 25, 2017. https://doi.org/10.7554/eLife.24463.

40. Lahiri, S., Chao, J.T., Tavassoli, S., Wong, A.K., Choudhary, V., Young, B.P., Loewen, C.J., and Prinz, W.A. (2014). A conserved endoplasmic reticulum membrane protein complex (EMC) facilitates phospholipid transfer from the ER to mitochondria. PLoS Biol. *12*, e1001969.

41. Nguyen, N., Francoeur, N., Chartrand, V., Klarskov, K., Guillemette, G., and Boulay, G. (2009). Insulin promotes the association of heat shock protein 90 with the inositol 1,4,5-trisphosphate receptor to dampen its Ca2+ release activity. Endocrinology *150*, 2190–2196.

42. Hedskog, L., Pinho, C.M., Filadi, R., Rönnbäck, A., Hertwig, L., Wiehager, B., Larssen, P., Gellhaar, S., Sandebring, A., Westerlund, M., et al. (2013). Modulation of the endoplasmic reticulum-mitochondria interface in Alzheimer's disease and related models. Proc. Natl. Acad. Sci. USA *110*, 7916–7921.

43. Allan, R.K., and Ratajczak, T. (2011). Versatile TPR domains accommodate different modes of target protein recognition and function. Cell Stress Chaperones *16*, 353–367.

44. Kuhn, S., Bussemer, J., Chigri, F., and Vothknecht, U.C. (2009). Calcium depletion and calmodulin inhibition affect the import of nuclear-encoded proteins into plant mitochondria. Plant J. *58*, 694–705.

45. Metallo, C.M. (2012). Expanding the reach of cancer metabolomics. Cancer Prev. Res. (Phila.) *5*, 1337–1340.

46. Sotgia, F., Whitaker-Menezes, D., Martinez-Outschoorn, U.E., Flomenberg, N., Birbe, R.C., Witkiewicz, A.K., Howell, A., Philp, N.J., Pestell, R.G., and Lisanti, M.P. (2012). Mitochondrial metabolism in cancer metastasis: Visualizing tumor cell mitochondria and the "reverse Warburg effect" in positive lymph node tissue. Cell Cycle *11*, 1445–1454.

47. Davis, F.M., Azimi, I., Faville, R.A., Peters, A.A., Jalink, K., Putney, J.W., Jr., Goodhill, G.J., Thompson, E.W., Roberts-Thomson, S.J., and Monteith, G.R. (2014). Induction of epithelial-mesenchymal transition (EMT) in breast cancer cells is calcium signal dependent. Oncogene *33*, 2307–2316.

48. Bauckman, K., Haller, E., Taran, N., Rockfield, S., Ruiz-Rivera, A., and Nanjundan, M. (2015). Iron alters cell survival in a mitochondria-dependent pathway in ovarian cancer cells. Biochem. J. *466*, 401–413.

49. Stoica, R., De Vos, K.J., Paillusson, S., Mueller, S., Sancho, R.M., Lau, K.F., Vizcay-Barrena, G., Lin, W.L., Xu, Y.F., Lewis, J., et al. (2014). ER-mitochondria associations are regulated by the VAPB-PTPIP51 interaction and are disrupted by ALS/FTD-associated TDP-43. Nat. Commun. *5*, 3996.

50. Falkevall, A., Alikhani, N., Bhushan, S., Pavlov, P.F., Busch, K., Johnson, K.A., Eneqvist, T., Tjernberg, L., Ankarcrona, M., and Glaser, E. (2006). Degradation of the amyloid beta-protein by the novel mitochondrial peptidasome, PreP. J. Biol. Chem. *281*, 29096–29104.

51. Wu, S., Sampson, M.J., Decker, W.K., and Craigen, W.J. (1999). Each mammalian mitochondrial outer membrane porin protein is dispensable: Effects on cellular respiration. Biochim. Biophys. Acta *1452*, 68–78.

52. Filadi, R., Greotti, E., Turacchio, G., Luini, A., Pozzan, T., and Pizzo, P. (2015). Mitofusin 2 ablation increases endoplasmic reticulum-mitochondria coupling. Proc. Natl. Acad. Sci. USA *112*, E2174–E2181.

53. Takano, T., Kohara, M., Kasama, Y., Nishimura, T., Saito, M., Kai, C., and Tsukiyama-Kohara, K. (2011). Translocase of outer mitochondrial membrane 70 expression is induced by hepatitis C virus and is related to the apoptotic response. J. Med. Virol. *83*, 801–809.

54. Pantazaka, E., and Taylor, C.W. (2011). Differential distribution, clustering, and lateral diffusion of subtypes of the inositol 1,4,5-trisphosphate receptor. J. Biol. Chem. *286*, 23378–23387.

55. Pinton, P., Rimessi, A., Romagnoli, A., Prandini, A., and Rizzuto, R. (2007). Biosensors for the detection of calcium and pH. Methods Cell Biol. *80*, 297–325.

56. Alzayady, K.J., Wang, L., Chandrasekhar, R., Wagner, L.E., 2nd, Van Petegem, F., and Yule, D.I. (2016). Defining the stoichiometry of inositol 1,4,5-trisphosphate binding required to initiate Ca2+ release. Sci. Signal. *9*, ra35.

57. Salabei, J.K., Gibb, A.A., and Hill, B.G. (2014). Comprehensive measurement of respiratory activity in permeabilized cells using extracellular flux analysis. Nat. Protoc. *9*, 421–438.

58. Filadi, R., Greotti, E., Turacchio, G., Luini, A., Pozzan, T., and Pizzo, P. (2016). Presenilin 2 modulates endoplasmic reticulum-mitochondria coupling by tuning the antagonistic effect of mitofusin 2. Cell Rep. *15*, 2226–2238.

59. Schreiner, B., and Ankarcrona, M. (2017). Isolation of mitochondria-associated membranes (MAM) from mouse brain tissue. Methods Mol. Biol. *1567*, 53–68.

STAR★METHODS

KEY RESOURCES TABLE

REAGENT or RESOURCE	SOURCE	IDENTIFIER
Antibodies		
mouse anti-TOM70	Novus Biologicals	Cat# H00009868-B01P; RRID:AB_1725263
rabbit anti-TOM70	Novus Biologicals	Cat# NB110-58347; RRID:AB_877738
Rabbit anti-TOM70	Santa Cruz Biotechnology	Cat# sc-366282
rabbit anti-TOM20	Santa Cruz Biotechnology	Cat# sc-11415; RRID:AB_2207533
mouse anti-TOM20	Santa Cruz Biotechnology	Cat# sc-17764; RRID:AB_628381
mouse anti-IP3R3	BD Biosciences	Cat# 610312; RRID:AB_397704
rabbit anti-IP3R3	Millipore	Cat# AB9076; RRID:AB_571029
rabbit anti-calnexin	Abcam	Cat# ab13504; RRID:AB_2040667
rabbit anti-VAPB (3503)	King's College London [49],	Produced and characterized by Professor Christopher Miller
Rabbit anti-PreP	Stockholm University [50],	Produced and characterized by Professor Elzbieta Glaser
rabbit anti-TOM40	Santa Cruz Biotechnology	Cat# sc-11414; RRID:AB_793274
goat anti-VDAC1	Santa Cruz Biotechnology	Cat# sc-8828; RRID:AB_793935
mouse anti-VDAC1	Abcam	Cat# ab14734; RRID:AB_443084
goat anti-COX1	Santa Cruz Biotechnology	Cat# sc-23982; RRID:AB_2084824
rabbit anti-GRP75	Santa Cruz Biotechnology	Cat# sc-13967; RRID:AB_647720
rabbit anti-LC3B	Cell signaling	Cat# 2775; RRID:AB_915950
mouse anti-Tubulin	Santa Cruz Biotechnology	Cat# sc-53646; RRID:AB_630403
mouse anti-actin	Sigma-Aldrich	Cat# A4700; RRID:AB_476730
rabbit anti-MCU	Sigma-Aldrich	Cat# HPA016480; RRID:AB_2071893
mouse anti-COX-IV	Thermo Fisher Scientific	Cat# 459600; RRID:AB_2532240
rabbit anti-P-PDH	Millipore	Cat# ABS204; RRID:AB_11205754
mouse anti-PDH	Santa Cruz Biotechnology	Cat# sc-377092
rabbit anti MPC1	Sigma-Aldrich	Cat# SAB4502158; RRID:AB_10745439
goat anti-ANT1/2/3	Santa Cruz Biotechnology	Cat# sc-9300; RRID:AB_2190366
rabbit anti-LDH-A	Abnova	Cat# H00003939-D01; RRID:AB_10720605
Gotal anti-FACL4 (ACSL4 (N-18))	Santa Cruz	Cat# sc-47977 RRID:AB_2222548
Chemicals, Peptides, and Recombinant Proteins		
BAPTA-AM	Thermo Fisher Scientific	Cat# B6769
ATP	Sigma-Aldrich	Cat# A9062-1G
Bradykinin	Calbiochem	Cat# 05-23-0500
Histamine	Sigma-Aldrich	Cat# H7250-5G
Baf A1	Sigma-Aldrich	Cat# B1793-10UG
Formalin solution, neutral buffered, 10%	Sigma-Aldrich	Cat# HT5011-1CS
Glutaraldehyde	Ladd Research Industries	Cat# 20100
LX-112 resin	Ladd Research Industries	Cat# LR21310
Percoll®	Sigma-Aldrich	Cat# P1644-100ML
Poly-D-lysine hydrobromide	Sigma-Aldrich	Cat# P7405-5MG
CHAPSO	Sigma-Aldrich	Cat# C3649-5G
Dynabeads Protein G for Immunoprecipitation	Thermo Fisher	Cat# 10004D
Dynabeads Protein A for Immunoprecipitation	Thermo Fisher	Cat# 10002D
Oligomycin-A	Sigma-Aldrich	Cat# 75351-5MG
FCCP	Sigma-Aldrich	Cat# C2920
Rotenone	Sigma-Aldrich	Cat# R8875-1G

(*Continued on next page*)

REAGENT or RESOURCE	SOURCE	IDENTIFIER
Antimycin-A	Sigma-Aldrich	Cat# A8674-25MG
Coelenterazine native	Biotium	Cat# 10110-1
Gramicidin-A	Abcam	Cat# 144510
Protein A/G plus Agarose	Santa Cruz Biotechnology	Cat# sc-2003
Critical Commercial Assays		
Duolink *In Situ* PLA Probe Anti-Mouse PLUS	Sigma-Aldrich	Cat# DUO92001
Duolink *In Situ* PLA Probe Anti-Mouse MINUS	Sigma-Aldrich	Cat# DUO92004
Duolink *In Situ* PLA Probe Anti-Rabbit PLUS	Sigma-Aldrich	Cat# DUO92002
Duolink *In Situ* PLA Probe Anti-Rabbit MINUS	Sigma-Aldrich	Cat# DUO92005
Duolink *In Situ* Mounting Medium with DAPI	Sigma-Aldrich	Cat# DUO82040-5ML
Pierce BCA Protein Assay Kit	Thermo Fisher	Cat# 23225
Pierce TM Protein A/G Magnetic Beads	Thermo Fisher	Cat# 88802
alamarBlue	ThermoFisher Scientific	Cat# DAL1025
Mitochondrial ToxGlo™	Promega	Cat# G8000
Experimental Models: Cell Lines		
Wt MEF	ATCC	Cat# CRL-2991
HeLa	ATCC	Cat# ATCC CCL-2
VDAC1/3 $^{-/-}$ MEF	[51]	N/A
IP3Rs-1/2/3-triple KO HEKs	Kerafast	Cat# EUR030
Experimental Models: Organisms/Strains		
Mouse: C57BL6/J	The Jackson Laboratory (Jax)	Cat# 000664
Oligonucleotides		
Control siRNA	Sigma Aldrich	Cat# SIC001
siRNA targeting sequence mouse TOM70 (A)	Sigma Aldrich	Cat# SASI_Mm01_00169128
siRNA targeting sequence mouse TOM70 (B)	Sigma Aldrich	Cat# SASI_Mm01_00169127
siRNA targeting sequence human TOM70	Sigma Aldrich	Cat# SASI_Hs01_00184261
siRNA targeting sequence mouse TOM20	Sigma Aldrich	Cat# SASI_Mm02_00327578
Recombinant DNA		
Mt-RFP	[52]	N/A
ER-GFP	[52]	N/A
Mt-YFP	[52]	N/A
TOM70-YFP	This paper	N/A
TOM70-myc	[53]	N/A
IP3R3-CFP	[54]	N/A
MCU	[31]	N/A
Cyt-Aequorin	[55]	N/A
Mt-mut Aequorin	[55]	N/A
MIMS Aequorin	[19]	N/A
OMM-YFP	[21]	N/A
OMM-RFP	[17]	N/A
D4ER	[20]	N/A
Nuclear ATeam1.03	[32]	N/A
Mitochondrial ATeam1.03	[32]	N/A
Software and Algorithms		
IBM SPSS Statistics 22.0	IMB Corporation	https://spss.en.softonic.com/
ImageJ	National Institutes of Health, Bethesda, MD, USA.	https://imagej.nih.gov/ij/download.html
Duolink ImageTool	Olink Bioscience, Sweden	DUO90806-1EA (currently distributed by Sigma-Aldrich)

CONTACT FOR REAGENT AND RESOURCE SHARING

Further information and requests for resources and reagents should be directed to and will be fulfilled by the Lead Contact, Paola Pizzo (paola.pizzo@unipd.it).

EXPERIMENTAL MODEL AND SUBJECT DETAILS

Animal models

For co-immunoprecipitation and subcellular fractionation, two to five wt female 10-week old C57BL6/J mice (weight 25 g) were used per experiment. Animals were kept in an enriched environment including bedding material to a maximum of 5 animals per cage. They had free access to water and food pellets and the day/night light cycle was 12/12 h with room temperature between 19-21°C. Animals were sacrificed by cervical dislocation. Brains were collected, stored in buffer on ice and subsequently homogenized. Ethical permission for was obtained by Stockholm South Ethical Committée (Dnr: S53-14).

Cell lines

HeLa and wt MEF cells were obtained from ATCC, HEK cells IP3Rs-1/2/3 triple KO were previously described [56] and obtained from Kerafast, $VDAC1/3^{-/-}$ MEF cells were gifts from Dr. Andrea Rasola (Dept of Biomedical Sciences, University of Padua, Italy).

HeLa, MEF and HEK cells were grown at 37°C in DMEM (Sigma # D5671), supplemented with 10% FCS, L-glutamine (2 mM), penicillin (100 U/mL) and streptomycin (100 µg/mL), in a humidified atmosphere containing 5% CO_2. Cells were seeded onto glass coverslips (13 or 18-mm diameter) and transfection was performed at 50% confluence using Lipofectamine 2000 Transfection Reagent (Life Technologies) in the case of MEF and HEK cells or TransIT-LT1 (MIRUS) for HeLa cells. Aequorin, FRET, Seahorse measurements, transmission electron microscopy and alamarBlue were performed 48 h after transfection. For RNAi experiments, Control-siRNA (MISSION siRNA Universal Negative Control #1 SIC001, Sigma Aldrich), TOM70-siRNA (SASI_Mm01_00169128 or SASI_Mm01_00169127 for mouse sequence, SASI_Hs01_00184261 for human sequence, Sigma Aldrich) or TOM20-siRNA (SASI_Mm02_00327578) were added to the transfection mixes to a final concentration of 50 nM. For the rescue experiments, a previously described human TOM70-myc encoding construct [53] was co-transfected with mouse-specific siRNAs in MEFs cells. The plasmids encoding ER and mitochondria-targeted fluorescent proteins were previously described [52], as well as those of cytosolic and mitochondrial aequorin [55], MIMS aequorin [19], D4ER [20], nuclear and mitochondrial ATeam1.03 [32], OMM-YFP [21], OMM-RFP [17], IP3R3-CFP [54]. TOM70-YFP was generated by subcloning TOM70 sequence within the BamHI site of YFP-pcDNA3.

All the KO cell lines were authenticated for the absence of the specific protein by western blot, while HeLa cells and wt MEFs were not authenticated.

METHOD DETAILS

Aequorin and GCAMP Ca^{2+} measurements

MEF cells (0.3×10^5) were plated on 13 mm diameter coverslips and, after 24 h, transfected with the cytosolic (cyt-Aeq), the low-affinity mitochondrial matrix (mit-Aeqmut, referred in the text as mit Aeq) or MIMS-Aequorin (mims-Aeq) encoding plasmids together with the indicated siRNA. 48 h after transfection, coverslips with cells were incubated with native coelenterazine (5 µM) for 1 h in KRB (Krebs–Ringer modified buffer, in mM: 140 NaCl, 2.8 KCl, 2 $MgCl_2$, 10 HEPES, 11 glucose, pH 7.4 at 37°C) supplemented with 1 mM $CaCl_2$, and then transferred to the perfusion chamber. All aequorin measurements were carried out in KRB at 37°C. The mix of IP3-generating agonists, added in Ca^{2+}-free, EGTA (500 µM)-containing KRB was: ATP (100 µM), Bradykinin (100 nM), Histamine (100 µM). The experiments were terminated by lysing the cells with 100 µM digitonin in a hypotonic Ca^{2+}-containing solution (10 mM $CaCl_2$ in H_2O), to consume the remaining aequorin pool. The light signal was collected by a photomultiplier (H7360-01 Hamamatsu Photonics), the output of the amplifier/discriminators was then captured by a photon counter (C8855-01 Hamamatsu Photonics) and recorded for analysis by the software (Hamamatsu Photonics). Signal was then calibrated into $[Ca^{2+}]$ as previously described [55], by exploiting the relationship between $[Ca^{2+}]$, the corresponding rate of light production (L) and the maximal rate of light production at saturating $[Ca^{2+}]$ (L_{max}).

For Ca^{2+} measurements upon Capacitive Ca^{2+} Entry (CCE) activation, cells were sequentially pre-treated with the mix of IP3-generating agonists described above and the SERCA inhibitor cyclopiazonic acid (CPA, 20 µM) for 6 min in a Ca^{2+}-free, EGTA (500 µM)-containing medium to completely release ER-Ca^{2+} content; cells were then perfused with the same medium without EGTA supplemented with $CaCl_2$ (5 mM).

In the experiments with permeabilized cells, an intracellular-like medium was used (in mM): 130 KCl, 10 NaCl, 1 KH_2PO_4, 2 succinic acid, 1 $MgSO_4$, 20 HEPES, 0.05 EGTA (pH 7 at 37 °C). Cells were permeabilized by perfusion (1 min) with 100 µM digitonin (added to the intracellular-like medium containing EGTA (50µM)), digitonin was removed by 2-min washing with the same solution without digitonin, and mitochondrial Ca^{2+} uptake was elicited by cells perfusion with the same intracellular solution without EGTA and containing $CaCl_2$ at different concentrations (5 or 10 µM). All the materials were from Sigma-Aldrich.

Evaluation of basal $[Ca^{2+}]$ within mitochondrial matrix in MEF or HEK cells was performed 48h after transfection with mitochondrial GCAMP6f, essentially as previously described [31]. Medium was replaced with KRB medium (see Aequorin measurements)

supplemented with FCS (1%). Fluorescence was recorded using an inverted microscope (Zeiss Axiovert 100) with a 40 × oil objective (Fluar, NA 1.30) in the 500-530 nm range (by using a band-pass filter from Chroma Technologies), by sequentially exciting GCAMP6f at 475 nm (the Ca^{2+}-sensitive wavelength) for 180 ms and at 410 nm (the Ca^{2+}-insensitive isosbestic point) for 300 ms. Excitation light was produced by a monochromator (polychrome V; TILL Photonics) and filtered with a 505 nm DRLP filter (Chroma Technologies). Acquisitions were performed every 5 s for 1 min. Images were background subtracted and analyzed with ImageJ. The ratio (R) between emissions measured by exciting at 475 nm and at 410 nm, respectively, was calculated by tracing ROIs comprising the entire mitochondrial network of each cells. R is proportional to $[Ca^{2+}]$ within a range of $[Ca^{2+}]$ near the K_d of the probe.

Oxygen consumption rate

1×10^4 wt MEF or HEK cells/well were seeded in 200 μL of DMEM (see above) in XF24 cell culture microplates (Seahorse Bioscience) and transfected after 24 h with either control-siRNA or TOM70-specific siRNA. 48 h after transfection, the medium was replaced with 670 μL of KRB medium (see Aequorin measurements) supplemented with FCS (5%). Where indicated, BAPTA-AM (5 μM) was added to this medium. Cells were incubated at 37°C for 30 min, and then oxygen consumption rate (OCR) was measured with an XF24 Extracellular Flux Analyzer (Seahorse Bioscience). After OCR baseline measurement, oligomycin (1 μg/mL), FCCP (1.2 μM) and rotenone (1 μM) plus antimycin A (1 μM) were sequentially added. In HEK cells, oligomycin was not added before FCCP (0.25 μM) because we observed it dampens FCCP-induced maximal respiration. After the experiments, cells were counted and data were normalized for cells number and expressed relatively to Controls baseline-OCR.

OCR measurements in permeabilized cells were performed essentially as previously described [57]. Briefly, 48h after transfection, MEF cells were permeabilized for 4 minutes with 25 μM digitonin in MAS buffer (in mM: 70 sucrose, 220 mannitol, 10 KH_2PO_4, 5 $MgCl_2$, 2 HEPES, 0.25 EGTA, pH 7.2 with KOH). Immediately before use, 200 mg fatty-acid- free BSA (Sigma Aldrich) was added to 50 mL of MAS buffer. After permeabilization, digitonin was removed and 670 μL of MAS buffer supplemented with fatty-acid-free BSA was added to each well of the XF24 cell culture microplate. Where indicated, substrates (in mM: 2 pyruvate, 5 succinate, 1 malate, 4 glutamate, pH 7.2 with KOH), ADP (0.5 mM, pH 7.2 with KOH) and rotenone (1 μM) plus antimycin A (1 μM) were sequentially added. OCR values were normalized for cells number and expressed relatively to controls baseline-OCR.

Mitochondrial Transmembrane Potential Measurements

Mitochondrial membrane potential (ψ_{mit}) was determined by tetramethyl rhodamine methyl ester (TMRM) fluorescent dye. Wt MEFs cell, transfected with a cytosolic-CFP encoding plasmid (to select only transfected cells) and with Control or TOM70-specific siRNA, were loaded for 30 min at RT with 10 nM TMRM, in KRB (see Aequorin measurements). TMRM fluorescence was recorded using an inverted microscope (Zeiss Axiovert 100) with a 40 × oil objective (Fluar, NA 1.30). Excitation light at 540 ± 7.5 nm was produced by a monochromator (polychrome V; TILL Photonics) and passed through a Zeiss TRITC filter (Emission 573-613 nm) and a dichroic mirror (565 DCXR). Where indicated, FCCP (1.5 μM) was added. Images were acquire by a cooled CCD camera (SensicamQE PCO). Filters and dichroics were from Chroma Technologies. Images were acquired every 30 s (60 ms exposure). Images were exported as TIFF, background subtracted and analyzed with ImageJ.

ATP and ER-Ca^{2+} FRET measurements

For ATP measurements, wt MEFs (0.7×10^5) were plated on 18 mm diameter coverslips and, after 24 h, transfected with the nuclear and the mitochondrial matrix ATeam1.03 encoding plasmids, together with the indicated siRNA and control (pcDNA3) or MCU-encoding plasmids. 6 hours after transfection, medium was replaced with glucose-free, galactose (10 mM)-containing medium (GIBCO 11966-025), supplemented with FCS (5%). 48 h after transfection, ATP measurements were performed by mounting coverslips into an open-topped chamber, maintaining cells in a glucose-free KRB (see Aequorin measurements) supplemented with $CaCl_2$ (1 mM) and with galactose (10 mM). Cells were analyzed using a DM6000 inverted microscope (Leica) with a 40 × oil objective (HCX Plan Apo, NA 1.25). The excitation light was produced by a 410nm LED (Led Engin LZ1-00UA00 LED) and was filtered and collected as previously described [58]. Images were acquired every 5 s. Where indicated, oligomycin (1.5 μM) was added. For the experiments with gramicidin, the same modified-KRB described above was used, but without $CaCl_2$, to avoid massive Ca^{2+} entry from the PM and mitochondrial Ca^{2+} overload, due to gramicidin-induced PM depolarization. ER-Ca^{2+} measurements with the FRET-based D4ER cameleon Ca^{2+} probe [20] were performed as previously described [58].

Offline analysis of FRET experiments was performed with ImageJ. YFP and CFP images were background-subtracted and analyzed selecting specific regions of interest (ROIs) on each cell. YFP/CFP emissions ratio (R) was calculated at each frame. Data are presented as mean ± SEM.

Transmission electron microscopy

Upon 48h after siRNA transfection cells were trypsinized, pelleted and fixed in 2.5% (V/V) glutaraldehyde in 0.1M phosphate buffer. Cells were then incubated for 2h in 2% OsO4, dehydrated in ethanol and acetone and embedded in LX-112 resin (Ladd, Burlington, VT, USA). Leica Ultracut UCT (Leica, Wien, Austria) was used to prepare ultrathin sections and the samples contrasted with uranyl acetate followed by lead citrate. Tecnai 12 BioTWIN transmission electron microscope (FEI Company, Eindhoven, the Netherlands) at 100 kV was used to examine the samples. Digital images were taken with a Veleta camera (Olympus Soft Imaging Solutions, GmbH, Münster, Germany) at a magnification of 20.500 ×. Mitochondria perimeter, as well as mitochondria-ER contacts number, length and

percentage of OMM in contact with ER were measured using ImageJ software (National Institutes of Health, Bethesda, MD, USA). Distances ≤ 30 nm between ER and mitochondria were considered as contacts.

Cell viability

alamarBlue (#DAL1025, ThermoFisher Scientific, Waltham, MA, USA) and Mitochondrial ToxGlo assay (#G8000, Promega) were used to measure cell viability according to the manufacturer's protocol. Briefly, upon 48h of siRNA treatment, cells were incubated with 1x alamarBlue solution for 30 min at 37°C. Media with alamarBlue was then collected and fluorescence measured (λex = 530-560nm, λem = 580-610nm). For the Mitochondrial ToxGlo assay, the cytotoxicity reagent was added to the cells upon 48h of siRNA treatment and incubated for 30 minutes at 37°C. Then, fluorescence was measured (λex = 485nm; λem = 525nm).

Subcellular fractionation of mouse brains

Brains from 10 weeks old female C57BL6/J mice were homogenized and subcellular fractionation performed as previously described [42, 59]. Briefly, brains were cut into small pieces and homogenized. The homogenate was centrifuged twice at 800 x g to remove nuclei and cell debris. After 9000 x g centrifugation crude mitochondrial pellet (P2) and S3 were collected. S3 was further centrifuged at 20 000 x g to generate the fraction "20 000 x g (P3)" containing PM and thereafter at 100 000 x g to generate "100 000 x g (P4)" containing ER. The crude mitochondrial fraction (P2) was put onto a 30% Percoll gradient and centrifuged at 100 000 x g for separation of mitochondria and MAM. The obtained fractions were solubilized in RIPA buffer (150 mM NaCl, 1% (v/v) Triton X-100, 0.5% (w/v) sodium deoxycholate, 0.1% (v/v) sodium dodecyl sulfate, 50 mM Tris pH 7.5; supplemented with EDTA-free protease inhibitor cocktail of Life Technologies) on ice for 30 min. Unsolubilized material was spun down at 4000 x g for 5 min at 4°C. After protein determination by the BCA Protein Assay kit (ThermoFisher Scientific) 25 μg protein of each fraction were subjected to SDS-PAGE and purity confirmed by immunostaining for marker proteins of different subcellular compartments.

Proximity ligation assay (PLA)

MEF cells were counted and diluted in DMEM supplemented with 10% FCS. 10x10⁴ cells were plated in the inner ring of a poly-D-lysine coated 35-mm glass-bottom plate (MatTek Corportation #P35G-0-20-C) for 24h. Cells were then fixed with 4% (v/v) formaldehyde solution for 10 min. Chemicals and solutions used for PLA were provided by Duolink PLA (Sigma-Aldrich). Membranes were permeabilized with 0.4% (w/v) CHAPSO for 10 min and blocked with Duolink blocking solution for 30 min at 37°C. Antibodies raised in different species were used to assess the specific proximity between IP3R3 (mouse) and Tom70 (rabbit) (IP3R3-TOM70) or IP3R3 (mouse) and TOM20 (rabbit) (IP3R3-TOM20) for 1h at 37°C. Positive and negative controls were incubated with only one of the previously mentioned antibodies. Species-specific Duolink PLA probes were added and incubated for 1h at 37°C. For positive controls, Duolink PLA probes targeted to the same species were used. Whereas, for negative controls, one of the Duolink PLA probes was targeted to the species of the primary antibody while the second one to a different species. Furthermore, Duolink Far Red Fluorescent Detection Reagents were added according to manufacturer's instructions, except for signal amplification which was performed for 150 min. Fluorescently labeled Alexa Fluor 488 Phalloidin (Thermo Fisher Scientific) was added to stain F-actin and samples mounted using Duolink Mounting Media with DAPI. Fluorescent dots were then observed with a confocal microscope (Nikon A1RSi point scanning confocal inverted microscope). Images were acquired using a 60x oil immersion objective and PLA signals quantified with Duolink ImageTool. To exclude background and set up the threshold of the signal, five random pictures per experiment were used. To calculate the fold increase between IP3R3-TOM70 and IP3R3-TOM20 signal, the measured PLA dots were normalized to those of the respective positive controls.

Co-immunoprecipitation

Crude mitochondrial fractions, containing both mitochondria and MAM, were isolated from 10 weeks old female C57BL6/J mice as described above. After removal of ER and PM fraction, crude mitochondria were resuspended in Buffer A (1 M HEPES pH 7.5, 50 mM KCl, 2 mM EGTA; supplemented with EDTA-free protease inhibitor cocktail, Life Technologies). After protein determination by the BCA™ Protein Assay kit, an appropriate amount of crude mitochondrial lysate was incubated with Protein A/G magnetic beads (Life Technologies) for 30 min at 4°C for pre-clearing. Capturing was performed by incubation of the supernatant from the pre-clearing step with mouse monoclonal antibodies against IP3R3 or TOM70 or mouse IgG as negative control over night at 4°C. Immunocomplexes were precipitated with Protein A/G magnetic beads and eluted with SDS-containing 2 × Laemmli buffer (Sigma-Aldrich). Immunoprecipitates were analyzed by SDS-PAGE and western blot. IP in MEFs was performed as previously described [58]. 400 μg of protein lysate obtained in modified RIPA buffer (150mM NaCl, 25mM Tris HCl, 1% NP40, 0.01% SDS, 0.05% Na-DOC, 1mM Na₂EDTA, protease inhibitor cocktail, pH 7.4) were pre-cleared with 1 μg of irrelevant mouse IgG together with 20 μL of protein A/G PLUS Agarose (sc-2003 Santa Cruz Biotechnology), by incubating at 4°C for 30 min on a rocker platform. Samples were then incubated overnight with the indicated antibodies and then adsorbed on 25 μL of protein A/G PLUS Agarose at 4°C for 3h. Immunoprecipitates were collected by centrifugation at 900 *rcf.* and washed 4 times with 0.1M NaCl plus protease inhibitors. Beads were re-suspended in 50 μL of Loading Buffer and incubated at 60°C for 10 min. Protein were separated by SDS-PAGE and probed with the indicated antibodies.

Western blot and immunostaining

Samples were analyzed by western blot. Briefly, 25 μg of protein per lane were subjected to SDS-PAGE (precast 4%–12% polyacrylamide gel, Lifetechnologies) and transferred to Nitrocellulose membrane (GE Healthcare). After incubation with primary protein-specific and secondary species-specific HRP-coupled antibodies (GE Healthcare), proteins were visualized by ECL reaction (Millipore) on sensitive films (GE Healthcare) or by the UVITEC Mini HD9 apparatus (Eppendorf).

Immunofluorescence (IF), confocal and STED microscopy, FRAP

For standard IF, 24 or 48 hours after transfection, HeLa and wt MEF cells were washed with PBS, fixed in 4% formaldehyde (10 min), washed with PBS and quenched with NH_4Cl (50 mM in PBS). Cells were permeabilized for 3 min with 0.1% Triton X-100 in PBS and blocked with a PBS solution containing 2% BSA, 10% goat serum and 0.2% gelatin for 45 min. Cells were incubated with primary antibodies diluted in blocking solution (1:150) (anti-TOM70 Santa Cruz # sc-366282 (Figure S1B), anti TOM70 Abnova # H00009868-B01P (Figure 1), anti-TOM20 Santa Cruz # sc-17764), anti-LDH-A Abnova # H00003939-D01 for 1h30' at RT and washed three times with the blocking solution. For IP3R3-staining, cells were incubated over night at 4°C with the primary antibody (BD Biosciences #610312) diluted (1:75) in a PBS solution containing 5% milk and 0.1% Triton. For LC3-staining, 48h after transfection MEF cells, grown in standard glucose-containing DMEM, were incubated for 2 h in galactose-containing medium (to minimize the contribution of glycolysis to total ATP levels) with or without the addition of bafilomycin A1 (100 nM). Fixation and processing were performed according to manufacturer's instructions (anti LC3B antibody, Cell signaling # 2775). AlexaFluor488/555/647-conjugated secondary antibodies (Life Technologies) were applied for 45 min at RT (1:300 dilution in blocking solution), coverslips were washed three times with the blocking solution, finally in PBS and mounted with Mowiol. Images were acquired on a Leica SP5-II confocal microscope by sequential acquisition of each channel (adjusting the photomultiplier gain to reduce background noise and avoid signal saturation), background-subtracted and gamma settings were improved with the automatic ImageJ plugin *enhance image.* However, the Manders' and Pearson's co-localization coefficients were calculated on raw images (background subtracted) without any modification, applying the ImageJ *Co-localization Analysis* plugin. Where indicated, a ROI was traced along single mitochondrial profile and the relative fluorescence for each channel plotted. For LC3 dots analysis, dots were counted with the Fiji *3D object counter* plugin, setting as threshold 2.5-fold the mean intensity of LC3 signal in each cell.

For measurements of co-localization with the ER-mt split GFP probe (SPLICS_L), OMM-RFP, TOM20 or TOM70 channel was background subtracted, a threshold corresponding to the mean fluorescence intensity (calculated for each cell) was applied and the % of pixels above the threshold co-localized with the split-GFP signal was calculated.

STED analysis was performed on a Leica TCS-II SP5 STED CW microscope, equipped with a 100x/1.4 N.A. Plan Apochromat objective. A WLL laser (488 nm line) was used to excite TOM20 or TOM70 labeled with an Alexa488 (LifeTechnologies) secondary antibody; HyD (Leica) was employed for signal collection. Images were background-subtracted and processed with the ImageJ plugin *enhance image*.

FRAP experiments were performed essentially as previously described [58]. Briefly, living IP3Rs-KO cells expressing TOM70-YFP (or OMM-YFP [21], with or without the co-expression of IP3R3-CFP, were bathed in mKRB (see Aequorin measurements) and illuminated on a Leica SP5 confocal microscope equipped with a 100X/1.4 N.A. oil objective. The WLL 514 nm line was used to excite YFP. The power of the laser was increased at 80% during the bleaching period. Bleaching was performed in a selected ROI within the mitochondrial network (3 × 3 μm). Images were acquired every 4 s (24 s for the pre-bleaching period, 120 s for the recovery period). The mobile fraction R was calculated as R = (Fa-F0)/(Fi-F0), where Fa is the fluorescence in the bleached region after recovery, Fi is the fluorescence in the ROI before bleaching, F0 is the fluorescence immediately after bleaching [29].

QUANTIFICATION AND STATISTICAL ANALYSIS

Statistical analysis of the data was performed using IBM SPSS Statistics 22.0 software (IMB Corporation, New York, NY, USA). All results are expressed as mean ± SEM. Significance was calculated by Mann-Whitney U-test; unless differently specified, n usually represents cells for single-cell experiments or coverslips/wells for cell population analysis. The criterion for statistical significance was established at $p < 0.05$ *, $p < 0.01$ **, $p < 0.001$ ***.